3D printable high-performance conducting polymer hydrogel for all-hydrogel bioelectronic interfaces

Tao Zhou [1,5,7], Hyunwoo Yuk [1,6,7] ✉, Faqi Hu[2], Jingjing Wu [1], Fajuan Tian [2], Heejung Roh [1], Zequn Shen [3], Guoying Gu [3], Jingkun Xu[2], Baoyang Lu [2] ✉ & Xuanhe Zhao [1,4] ✉

Owing to the unique combination of electrical conductivity and tissue-like mechanical properties, conducting polymer hydrogels have emerged as a promising candidate for bioelectronic interfacing with biological systems. However, despite the recent advances, the development of hydrogels with both excellent electrical and mechanical properties in physiological environments is still challenging. Here we report a bi-continuous conducting polymer hydrogel that simultaneously achieves high electrical conductivity (over 11 S cm^{-1}), stretchability (over 400%) and fracture toughness (over 3,300 J m^{-2}) in physiological environments and is readily applicable to advanced fabrication methods including 3D printing. Enabled by these properties, we further demonstrate multi-material 3D printing of monolithic all-hydrogel bioelectronic interfaces for long-term electrophysiological recording and stimulation of various organs in rat models.

Electrically conductive hydrogels have emerged as promising alternatives to conventional metallic electrodes for bioelectronic interfaces owing to their unique combination of similarity to biological tissues (high water contents, softness) and electrical conductivity[1]. In particular, conducting polymer hydrogels—electrically conductive hydrogels based on conducting polymers—show a set of advantages over other conductive hydrogels based on concentrated ionic salts[2,3], metals[4,5] (for example, Ag, Au, Pt) or carbon nanomaterials[6] (for example, carbon nanotubes, graphene and its derivatives) including favourable electrical properties, stability in physiological environments, biocompatibility and fully organic characteristics[1,7,8].

Despite the recent advances in mechanically robust tough hydrogels mimicking biological tissues[9–13], the development of mechanically robust conducting polymer hydrogels has faced lingering challenges. Existing tough conducting polymer hydrogels, often prepared by mixing or polymerizing conducting polymers within tough hydrogel matrices, show low electrical conductivity below 0.3 S cm^{-1} due to low connectivity between electrical phases in the hydrogels[14–17] and/or high stiffness and low water contents dissimilar to biological tissues[15,18] (Supplementary Table 1). Attempts to achieve high electrical conductivity by increasing the conducting polymer contents (for example, pure conducting polymer hydrogels) substantially compromise the mechanical properties of hydrogels[19–21] (Supplementary Table 1), limiting their utility as bioelectronic interfaces that necessitate favourable mechanical and electrical properties simultaneously. Furthermore, many existing conducting polymer hydrogels are not applicable to

[1]Department of Mechanical Engineering, Massachusetts Institute of Technology, Cambridge, MA, USA. [2]Flexible Electronics Innovation Institute, Jiangxi Key Laboratory of Flexible Electronics, Jiangxi Science and Technology Normal University, Nanchang, China. [3]Robotics Institute, School of Mechanical Engineering, State Key Laboratory of Mechanical System and Vibration, Shanghai Jiao Tong University, Shanghai, China. [4]Department of Civil and Environmental Engineering, Massachusetts Institute of Technology, Cambridge, MA, USA. [5]Present address: Department of Engineering Science and Mechanics, Center for Neural Engineering, The Pennsylvania State University, University Park, PA, USA. [6]Present address: SanaHeal, Inc, Cambridge, MA, USA. [7]These authors contributed equally: Tao Zhou, Hyunwoo Yuk. ✉e-mail: hyunwooyuk@sanaheal.com; luby@jxstnu.edu.cn; zhaox@mit.edu
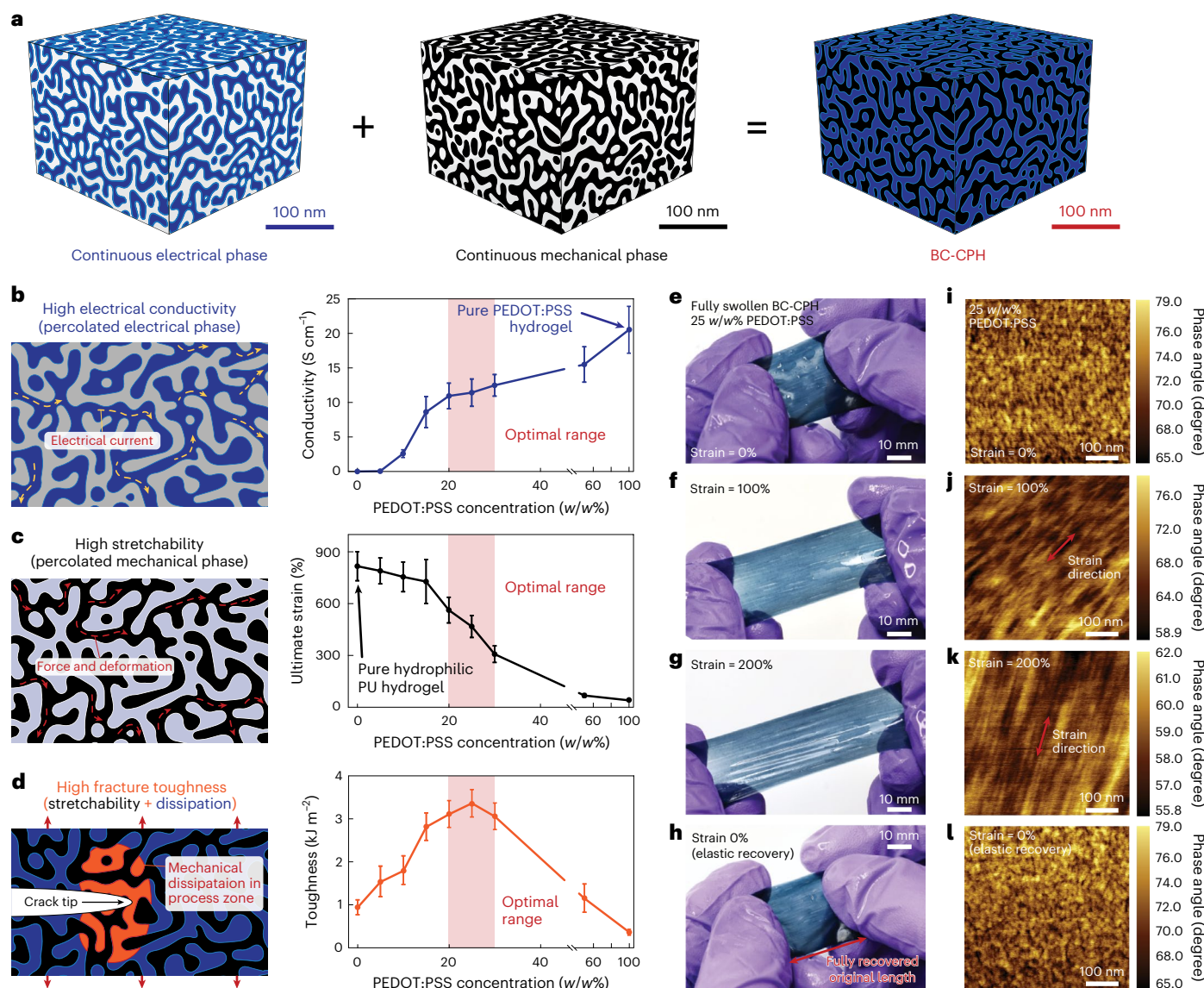
Fig. 1 | Design and implementation of the BC-CPH. a, Schematic illustrations of a BC-CPH consisting of an electrical phase based on PEDOT:PSS and a mechanical phase based on hydrophilic polyurethane (PU). **b–d**, Schematic illustrations for mechanisms (left) and plots (right) for electrical conductivity (**b**), ultimate strain (**c**) and fracture toughness (**d**) versus PEDOT:PSS concentration in the BC-CPH. **e–h**, Images of the fully swollen BC-CPH with 25 w/w% PEDOT:PSS at engineering strain of 0% (**e**), 100% (**f**), 200% (**g**) and 0% after full elastic recovery (**h**). **i–l**, Corresponding AFM phase images of the BC-CPH with 25 w/w% PEDOT:PSS at engineering strain of 0% (**i**), 100% (**j**), 200% (**k**) and 0% after full elastic recovery (**l**). Values in **b–d** represent the mean and the standard deviation ($n = 4$; independent samples). Each experiment was repeated independently three times.

advanced manufacturing techniques for hydrogels such as 3D printing, rendering them inappropriate for fabrication of bioelectronic devices (Supplementary Table 1).

Here we report a bi-continuous conducting polymer hydrogel (BC-CPH) to overcome these challenges by achieving high conductivity without sacrificing its mechanical properties. The BC-CPH can be prepared readily from phase-separated inks consisting of electrical phase (PEDOT:PSS) and mechanical phase (hydrophilic polyurethane) (Supplementary Fig. 1), allowing the use of various advanced fabrication strategies including spin-coating and electrospinning (low-viscosity ink) as well as micro-moulding and 3D printing (high-viscosity ink). The resultant BC-CPH (Fig. 1a) simultaneously achieves high electrical conductivity (over 11 S cm^{-1}), stretchability (over 400%), fracture toughness (over 3,300 J m^{-2}), water contents (~80%) and tissue-like softness (Young's modulus below 1 MPa) in physiological environments (Supplementary Table 1 and Supplementary Fig. 2).

Design and implementation of the BC-CPH

To implement the BC-CPH, we select PEDOT:PSS as an electrical phase and hydrophilic polyurethane as a mechanical phase dissolved in a mixed solvent consisting of water and ethanol (Extended Data Fig. 1). Owing to the different solubility of hydrophilic polyurethane and PEDOT:PSS in ethanol and water, hydrophilic polyurethane shows phase separation in the mixed solvent with less than 70 v/v% ethanol concentration (Extended Data Fig. 1a–e), whereas PEDOT:PSS shows phase separation in the mixed solvent with higher than 70 v/v% ethanol concentration (Extended Data Fig. 1f–j). Notably, both hydrophilic polyurethane and PEDOT:PSS are moderately phase separated without substantial aggregation and precipitation in the mixed solvent with 70 v/v% ethanol and 30 v/v% water (Extended Data Fig. 1b,g). As a result, the BC-CPH ink prepared based on the mixed solvent with 70 v/v% ethanol concentration shows a unique ink-level phase separation of both mechanical phase and electrical phase (Extended Data Fig. 1k).
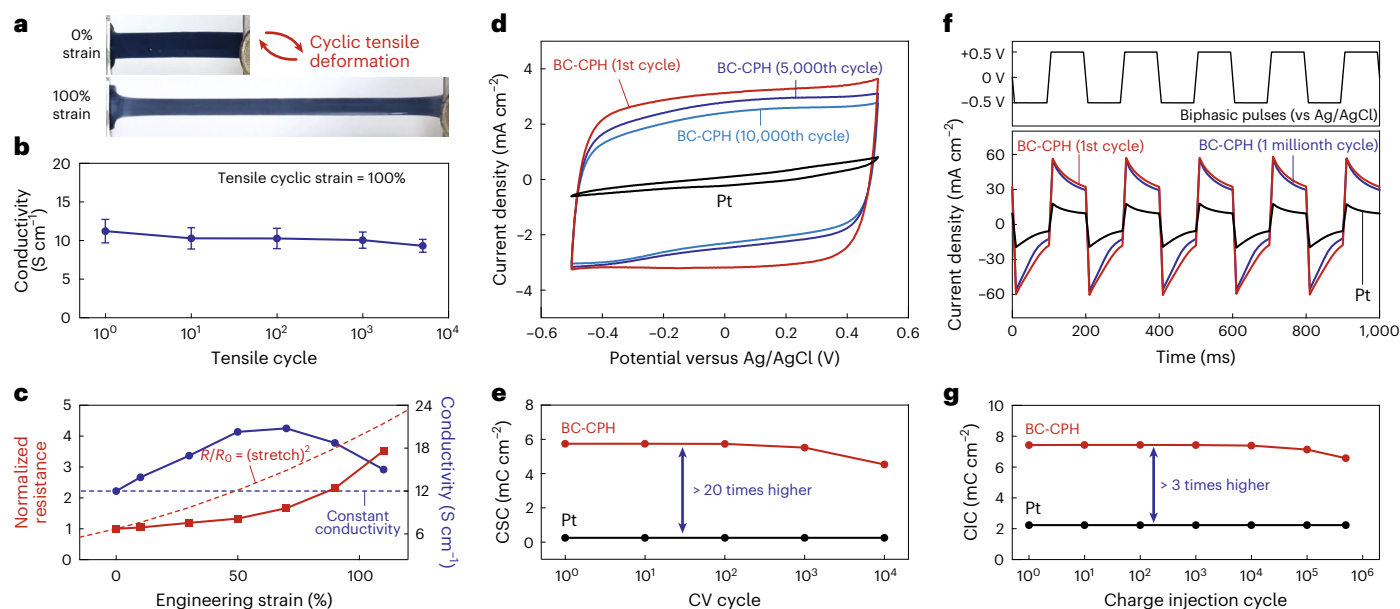
Fig. 2 | Electrical properties and stability of the BC-CPH. a, Images of the BC-CPH under cyclic tensile deformation of 100% engineering strain. **b**, Electrical conductivity versus tensile cycle of the BC-CPH. **c**, Plots for electrical resistance normalized to the resistance of non-deformed state (R/R_0, left axis) and electrical conductivity (right axis) versus engineering strain of the BC-CPH. Stretch is engineering strain plus unity. **d**, Current density versus potential plots for a Pt electrode and the BC-CPH at 1st, 5,000th and 10,000th cycles. **e**, CSC versus cyclic voltammetry (CV) cycle for a Pt electrode and the BC-CPH. **f**, Biphasic input pulses (top) and the corresponding current density versus time plots (bottom) for a Pt electrode and the BC-CPH at 1st and 1 millionth cycles. **g**, CIC versus charge injection cycle for a Pt electrode and the BC-CPH. Values in **b** represent the mean and the standard deviation ($n = 4$; independent samples).

The BC-CPH can be readily prepared by evaporating the solvent from the ink at room temperature followed by equilibration in wet physiological environments (see Methods for the detailed process of the BC-CPH preparation). During the solvent evaporation, the phase-separated mechanical and electrical phases in the BC-CPH ink are compacted to form bi-continuous phases, respectively (Fig. 1a,i). In contrast, conventional hydrophilic polymers used as a mechanical phase in conducting polymer hydrogels (for example, polyvinyl alcohol, polyacrylamide, polyacrylic acid) are soluble in water, resulting in homogeneously dispersed conducting polymer phase within the polymer solution without the pre-formed phase separation between mechanical and electrical phases[6,8,9,14,15]. Hence, the resultant conducting polymer hydrogels show either poor connectivity (in low conducting polymer concentration; Supplementary Fig. 3a) or aggregation (in high conducting polymer concentration; Supplementary Fig. 3b) of the conducting polymer phase, showing strong trade-offs between electrical and mechanical properties (Supplementary Fig. 4). The BC-CPH prepared from the ink with low PEDOT:PSS concentration results in a low connectivity between electrical phases (Supplementary Fig. 5a) and low electrical conductivity (Fig. 1b). Conversely, the BC-CPH prepared from the ink with high PEDOT:PSS concentration shows a low connectivity between mechanical phases (Supplementary Fig. 5c) and low stretchability (Fig. 1c and Supplementary Fig. 6). We find that an optimal range of PEDOT:PSS concentration (20–30 w/w%) provides bi-continuous presence of both mechanical and electrical phases in the BC-CPH (Fig. 1i and Supplementary Fig. 5b), simultaneously achieving high electrical conductivity (Fig. 1b) and stretchability (Fig. 1c and Supplementary Fig. 7). Notably, the removal of the mechanical phase by dissolving away hydrophilic polyurethane from the BC-CPH provides a stable free-standing PEDOT:PSS hydrogel, further confirming the presence of bi-continuous electrical and mechanical phases in the BC-CPH (Supplementary Fig. 8).

The BC-CPH shows fully recoverable elastic deformation over 200% strain (Fig. 1e–h) maintaining its bi-continuous phases (Fig. 1i–l) without plastic deformation[22]. Furthermore, the BC-CPH with the optimal range of PEDOT:PSS concentrations also shows a much higher fracture toughness over 3,000 J m^{-2} than mechanical or electrical phase-dominated hydrogels (Fig. 1d and Supplementary Fig. 9). This marked enhancement in fracture toughness of the BC-CPH may originate from a similar mechanism to other tough hydrogels[9,10,23], where the less stretchable PEDOT:PSS phase acts as a mechanical dissipater and the highly stretchable hydrophilic polyurethane phase maintains the integrity and elasticity of the BC-CPH (Fig. 1d).

Electrical properties and stability

The BC-CPH can provide favourable electrical and electrochemical properties including high electrical conductivity (over 11 S cm^{-1}) even after over 5,000 cycles of 100% tensile strain (Fig. 2a,b), low impedance (Supplementary Fig. 10a), high charge storage capacity (CSC) over 20 times higher than a Pt electrode (Fig. 2d,e) and high charge injection capacity over 3 times higher than a Pt electrode (Fig. 2f,g). The BC-CPH shows mixed electronic and ionic conductivity with higher contribution from the electronic conductivity[24] ($R_{electrolyte}/R_{polymer} = 4.24$) compared with Pt electrode (Supplementary Fig. 10c,e). The BC-CPH maintains favourable electrical and mechanical properties over 10,000 charging and discharging cycles (Fig. 2e), over 1 M biphasic charge injections (Fig. 2g), over 180 days of storage in phosphate buffered saline (PBS) (Extended Data Fig. 2) and over 28 days of storage in PBS with enzymes at 37 °C (Supplementary Fig. 11). Notably, the BC-CPH shows strain-insensitive electrical resistance under moderate strain up to 50% (Fig. 2c), potentially due to dynamic aggregation and alignment of the electrical phase in the deformed state[25,26] (Supplementary Fig. 12).

Applicability to diverse fabrication methods

The design of BC-CPH allows simple and facile fabrication from a viscous ink, which is readily applicable to various fabrication methods. The viscosity of the BC-CPH ink can be easily tuned by controlling the amount of solvent (70 v/v% ethanol and 30 v/v% water) in the ink (Fig. 3a). Notably, the ink-level phase separation of mechanical and
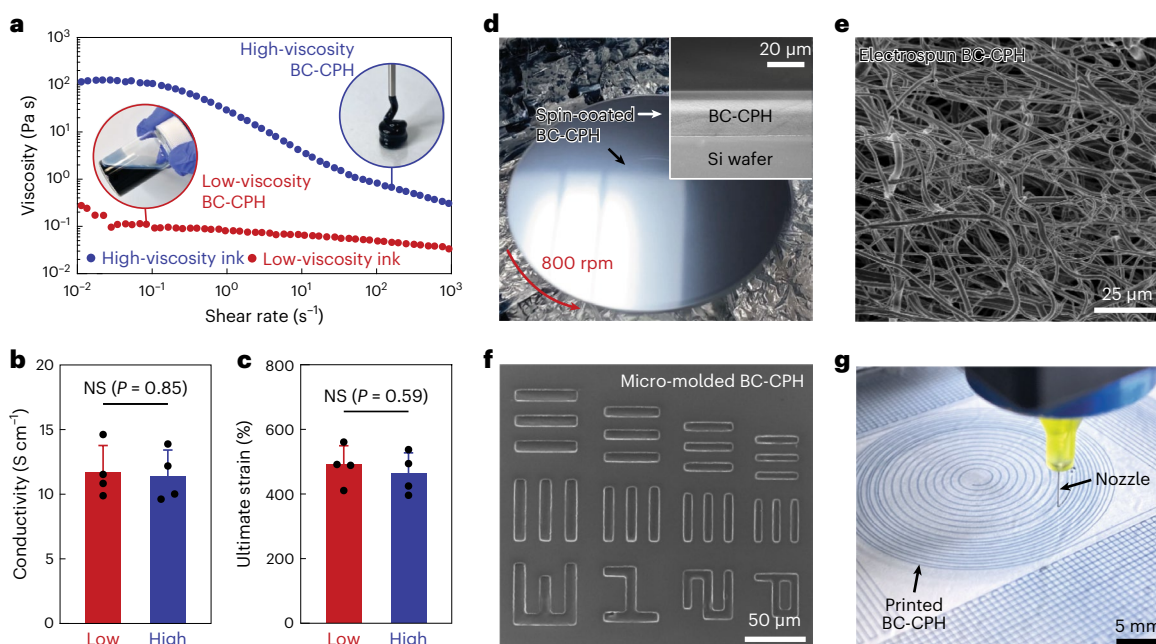
Fig. 3 | Applicability to diverse fabrication methods. a, Viscosity versus shear rate plots for the BC-CPH inks with high and low viscosity. Insets: the high-viscosity (inside blue circle) and low-viscosity (inside red circle) BC-CPH inks. **b,c**, Electrical conductivity (**b**) and ultimate strain (**c**) of the BC-CPH prepared from high and low-viscosity inks. **d**, Image of the spin-coated low-viscosity BC-CPH ink. Top-right inset: SEM image is the cross-sectional view of the spin-coated BC-CPH on a silicon wafer. **e**, SEM image of the electrospun low-viscosity BC-CPH ink. Each experiment was repeated independently 4 times. **f**, SEM image of the micro-moulded high-viscosity BC-CPH ink from a SU-8 soft lithography mould. **g**, Image of the 3D-printed high-viscosity BC-CPH ink. Values in **b** and **c** represent the mean and the standard deviation (*n* = 4; independent samples). Statistical significance and *P* values are determined by two-sided unpaired *t*-test; NS, not significant.

electrical phases and subsequent solvent evaporation-driven compaction into bi-continuous phases allow the resultant BC-CPH prepared from varying viscosity of inks to keep the consistent electrical and mechanical properties (Fig. 3b,c and Supplementary Fig. 13). The low-viscosity BC-CPH ink can be used in various manufacturing methods including spin-coating[20] (Fig. 3d) and electrospinning[27] (Fig. 3e). The high-viscosity BC-CPH ink shows favourable rheological properties as a mouldable and printable material, allowing fabrication of BC-CPH microstructures by micro-moulding based on soft lithography (Fig. 3f)[28] as well as by 3D printing[17,26,29] (Fig. 3g).

All-hydrogel bioelectronic interfaces

Taking advantage of the BC-CPH's ready applicability to multi-material 3D printing, we demonstrate printing-based fabrication of all-hydrogel bioelectronic interfaces (Fig. 4a). In combination with printable bioadhesive (Extended Data Fig. 3, Supplementary Figs. 14a and 15 and Supplementary Discussion 1) and insulating (Supplementary Figs. 14b, 16 and 17 and Supplementary Discussion 2) hydrogel inks, the BC-CPH enables multi-material printing-based fabrication of all-hydrogel bioelectronic interfaces with tissue-like softness and water contents[30,31] (Fig. 4b) in less than 10 min (Supplementary Fig. 18 and Supplementary Video 1). The printed bioelectronic interfaces take the form of monolithic hydrogels (electrodes by the BC-CPH, encapsulation by the insulating hydrogel and bio-integration by the bioadhesive hydrogel) with tissue-like softness and high flexibility in physiological environments (Fig. 4c and Supplementary Fig. 19).

Owing to the high stretchability of the BC-CPH and other constituent hydrogels (Supplementary Figs. 7 and 20), the all-hydrogel bioelectronic interfaces can withstand over 150% strain without failure (Fig. 4d). The bioadhesive in the all-hydrogel bioelectronic interfaces further provides rapid, robust and sutureless integration to the target tissues[32–34] (Fig. 4e, Extended Data Fig. 3 and Supplementary Video 2). The adhered interface can also be atraumatically detached on demand from the target tissue by application of a detachment solution without causing tissue damage[35] (Supplementary Fig. 15 and Supplementary Video 3).

The all-hydrogel bioelectronic interfaces maintain stable single-electrode impedance around 5 kΩ over 10,000 cycles of 20% tensile strain (Fig. 4f and Supplementary Fig. 21), over 56 days of storage in PBS (Fig. 4g and Extended Data Fig. 4) and over 28 days of storage in PBS with enzymes at 37 °C (Supplementary Fig. 22). Taking advantage of the strain-insensitive electrical resistance of the BC-CPH at moderate deformation (Fig. 2c), the all-hydrogel bioelectronic interfaces also show stable impedance up to 40% tensile strain (Fig. 4h and Extended Data Fig. 4a), which can be highly favourable for bioelectronic interfacing in dynamic physiological environments[6,36].

In vivo electrophysiological recording and stimulation

We conduct electrophysiological recording of rat hearts (Fig. 5a–f) and stimulation of rat sciatic nerves (Fig. 5g–n) and spinal cords (Extended Data Fig. 5) by the all-hydrogel bioelectronic interfaces to demonstrate their long-term in vivo bioelectronic interfacing capability. Multi-material 3D printing allows a flexible choice of designs and fast manufacturing of the all-hydrogel bioelectronic interfaces for various target organs (Supplementary Fig. 23). Favourable electrical properties of the BC-CPH electrodes in the all-hydrogel bioelectronic interfaces provide successful in vivo electrophysiological recording of rat hearts (epicardial signals, Fig. 5d) and stimulation of sciatic nerves (hindlimb movements, Fig. 5j,l) and rat spinal cords (forelimb movements, Extended Data Fig. 5d,f) on day 0 post-implantation.

Owing to low cytotoxicity (Supplementary Fig. 24), tissue-like properties and stability in physiological environments, the all-hydrogel bioelectronic interfaces show stable integration to the target tissues (Supplementary Fig. 25) and favourable tissue response during long-term in vivo implantation
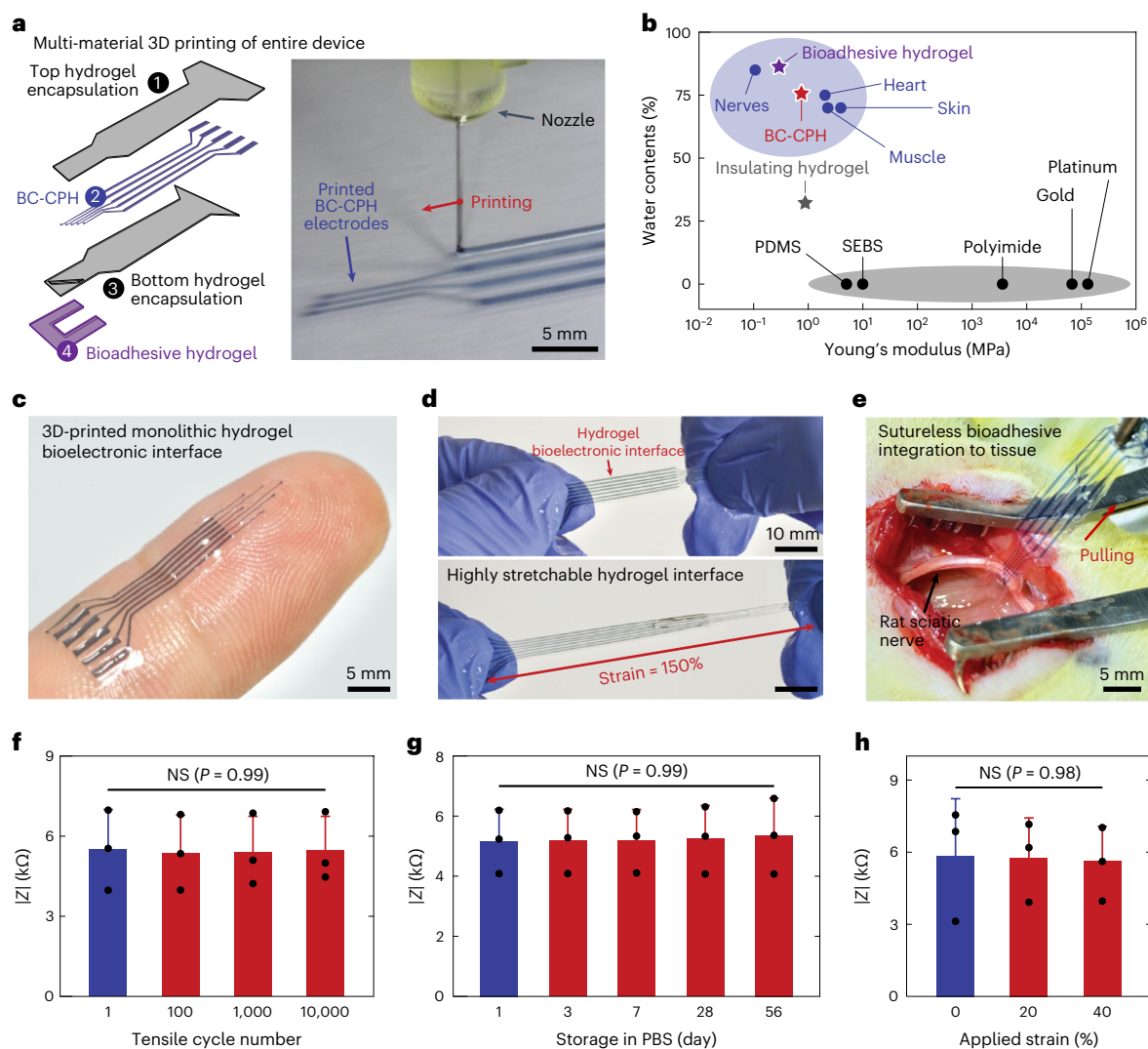
Fig. 4 | All-hydrogel bioelectronic interfaces. a, Schematic illustration (left) and image (right) of multi-material 3D printing-based fabrication of the all-hydrogel bioelectronic interface. **b**, Young's modulus versus water contents for the all-hydrogel bioelectronic interface (BC-CPH, insulating and bioadhesive hydrogels), conventional electrode and encapsulation materials, and biological tissues[31]. SEBS, styrene ethylene butylene styrene. **c**, Image of the all-hydrogel bioelectronic interface on a fingertip. **d**, Images of the highly stretchable all-hydrogel bioelectronic interface before (top) and after (bottom) deformation.

e, Image of sutureless robust bioadhesive integration of the all-hydrogel bioelectronic interface on a rat sciatic nerve. **f–h**, Impedance of one electrode channel in the all-hydrogel bioelectronic interface at 1 kHz under varying tensile cycle (**f**), storage time in a PBS bath at 37 °C (**g**) and tensile strain (**h**). Values in **f–h** represent the mean and the standard deviation (*n* = 3; independent samples). Statistical significance and *P* values are determined by one-way ANOVA followed by Bonferroni's multiple comparison test; NS, not significant.

over 2 months (Fig. 6). Histological analysis by a blinded pathologist indicates that the all-hydrogel bioelectronic interfaces elicit very mild inflammation to the target tissues (Fig. 6a–c) with fibrotic tissues around the all-hydrogel bioelectronic interfaces significantly thinner than those around elastomer-based control devices (that is, devices with polydimethylsiloxane (PDMS)-based encapsulation) and comparable to the sham group (Fig. 6d).

We further perform immunofluorescence analysis for various markers to evaluate tissue damage including neurofilament (Fig. 6e–l and Supplementary Figs. 26, 27 and 29) and foreign body response including fibroblasts (αSMA; Fig. 6e–l and Supplementary Figs. 26–28), macrophages (CD68; Fig. 6e–l and Supplementary Figs. 26–29), collagen (collagen I; Fig. 6e–l and Supplementary Figs. 26–28) and T cells (CD3; Supplementary Fig. 28). The quantitative analysis of fluorescence intensity indicates that the all-hydrogel bioelectronic interfaces elicit comparable expression of all markers to the sham group on days 7, 28 and 56 post-implantations on rat sciatic nerves

(Fig. 6i–l, Supplementary Figs. 26 and 27). In contrast, the elastomer-based control devices induce significantly lower expression of neurofilament and higher expression of αSMA, collagen I and CD68 compared with the sham group on day 28 post-implantation, indicating potential damage of neural tissues and higher foreign body response (Fig. 6i–l).

Enabled by the favourable in vivo biocompatibility and stability, the all-hydrogel bioelectronic interfaces can provide stable long-term electrophysiological recording and stimulation of rat hearts (Fig. 5e and Supplementary Fig. 30), sciatic nerves (Fig. 5k,m and Supplementary Fig. 31) and spinal cords (Extended Data Fig. 5 and Supplementary Fig. 32). Notably, the efficacy of electrophysiological recording and stimulation by the all-hydrogel bioelectronic interfaces increases in the longer term compared with the efficacy on day 0 (that is, right after implantation). The measured epicardial signals for heart recording (Fig. 5f) on day 28 post-implantation shows significantly higher signal-to-noise ratio (SNR) compared
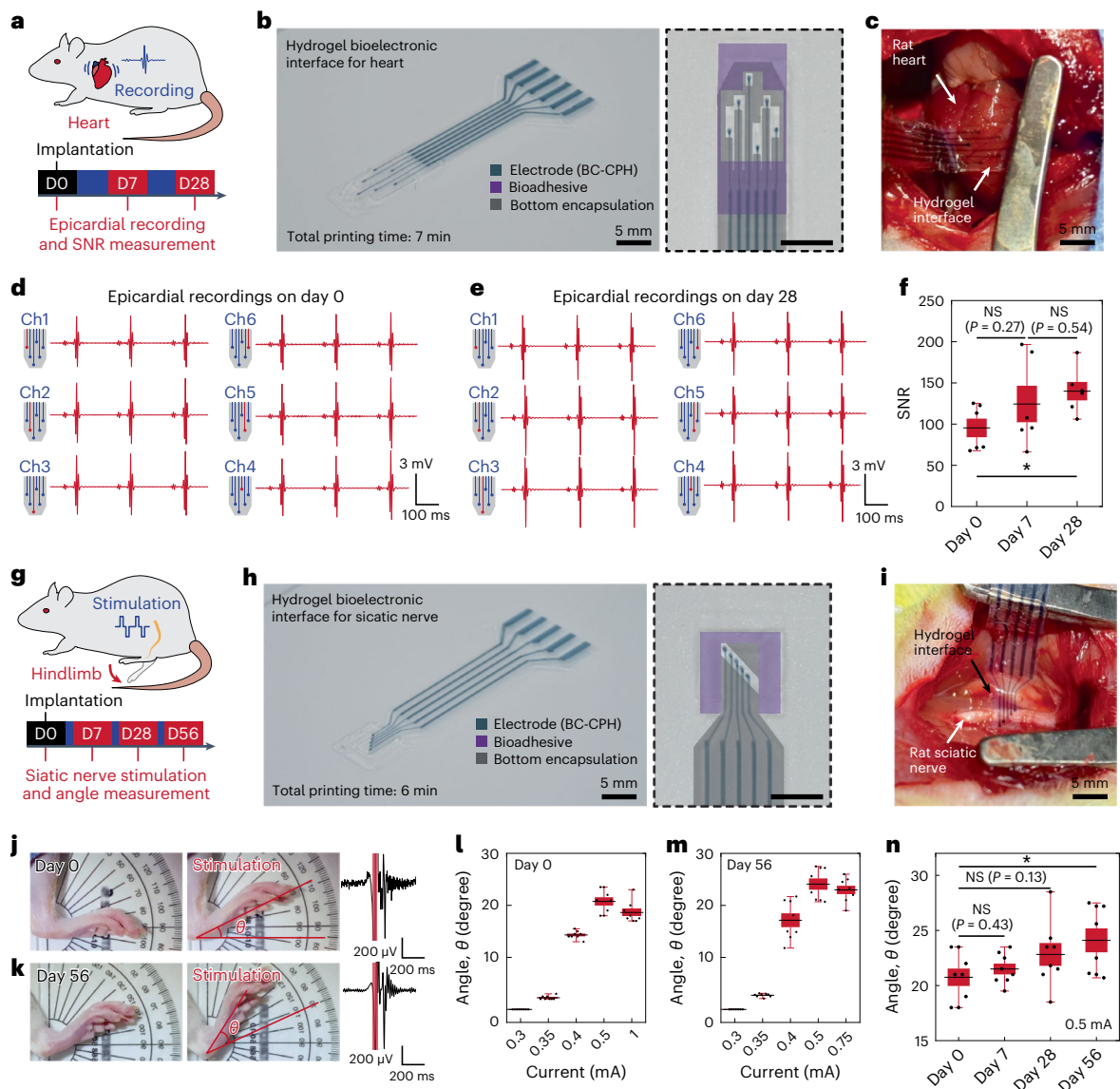
Fig. 5 | In vivo electrophysiological recording and stimulation. a,g, Schematic illustrations for rat heart recording (**a**) and sciatic nerve stimulation (**g**) by the all-hydrogel bioelectronic interfaces. **b,h**, Images of the printed all-hydrogel bioelectronic interfaces for heart (**b**) and sciatic nerve (**h**) in the overall view (left) and the magnified view of electrodes (right). Different materials are marked with colour overlays in the magnified view. **c,i**, Images of the implanted all-hydrogel bioelectronic interfaces on rat heart (**c**) and sciatic nerve (**i**). **d,e**, Epicardial recordings by different channels in the all-hydrogel bioelectronic interface on day 0 (**d**) and day 28 (**e**) post-implantation. **f**, Comparison of the SNR for epicardial recordings on day 0, day 7 and day 28 post-implantation. **j,k**, Images of rat hindlimb before (left) and after (middle) electrophysiological stimulation of the sciatic nerve by the all-hydrogel bioelectronic interface with corresponding

EMG recordings (right) on day 0 (**j**) and day 56 (**k**) post-implantation. The red-shaded regions in the EMG recordings indicate the stimulation pulses. **l,m**, Rat hindlimb movement angles upon sciatic nerve stimulations by the all-hydrogel bioelectronic interface at varying stimulation currents on day 0 (**l**) and day 56 (**m**) post-implantation. **n**, Comparison of the rat hindlimb movement angles on day 0, day 7, day 28 and day 56 post-implantation with stimulation current of 0.5 mA. In box plots (**f** and **l–n**), centre lines represent the mean, box limits delineate the standard error and whiskers reflect the 5th and 95th percentiles ($n = 6$ for **f**; $n = 8$ for **i–n**; independent experiments). Statistical significance and P values are determined by two-sided unpaired t-test; NS, not significant; *$P < 0.05$ (in **f**, $P = 0.019$; in **n**, $P = 0.026$).

with day 0 post-implantation. Significantly higher hindlimb joint angle movement for sciatic nerve stimulation on day 56 compared with day 0 post-implantation (Fig. 5n) and significantly larger forelimb movement distance for spinal cord stimulation on day 7 and day 28 compared with day 0 post-implantation (Extended Data Fig. 5h) for the same injected current are observed. This enhancement in long-term electrophysiological efficacy might be facilitated by the tissue-like properties, atraumatic bioadhesive integration and resultant favourable tissue interaction of the all-hydrogel bioelectronic interfaces[33,37].

Outlook

By addressing the lingering challenges in conductive hydrogels, the BC-CPH provides a promising material for tissue-like bioelectronic interfaces. Enabled by the unique set of advantages of the BC-CPH, we 3D print monolithic all-hydrogel bioelectronic interfaces capable of long-term high-efficacy electrophysiological stimulation and recording of diverse tissues and organs in rat models. This work may offer a versatile tool and platform not only for a vision of hydrogel bioelectronics[1] to achieve better electrical interfacing between machines and biological
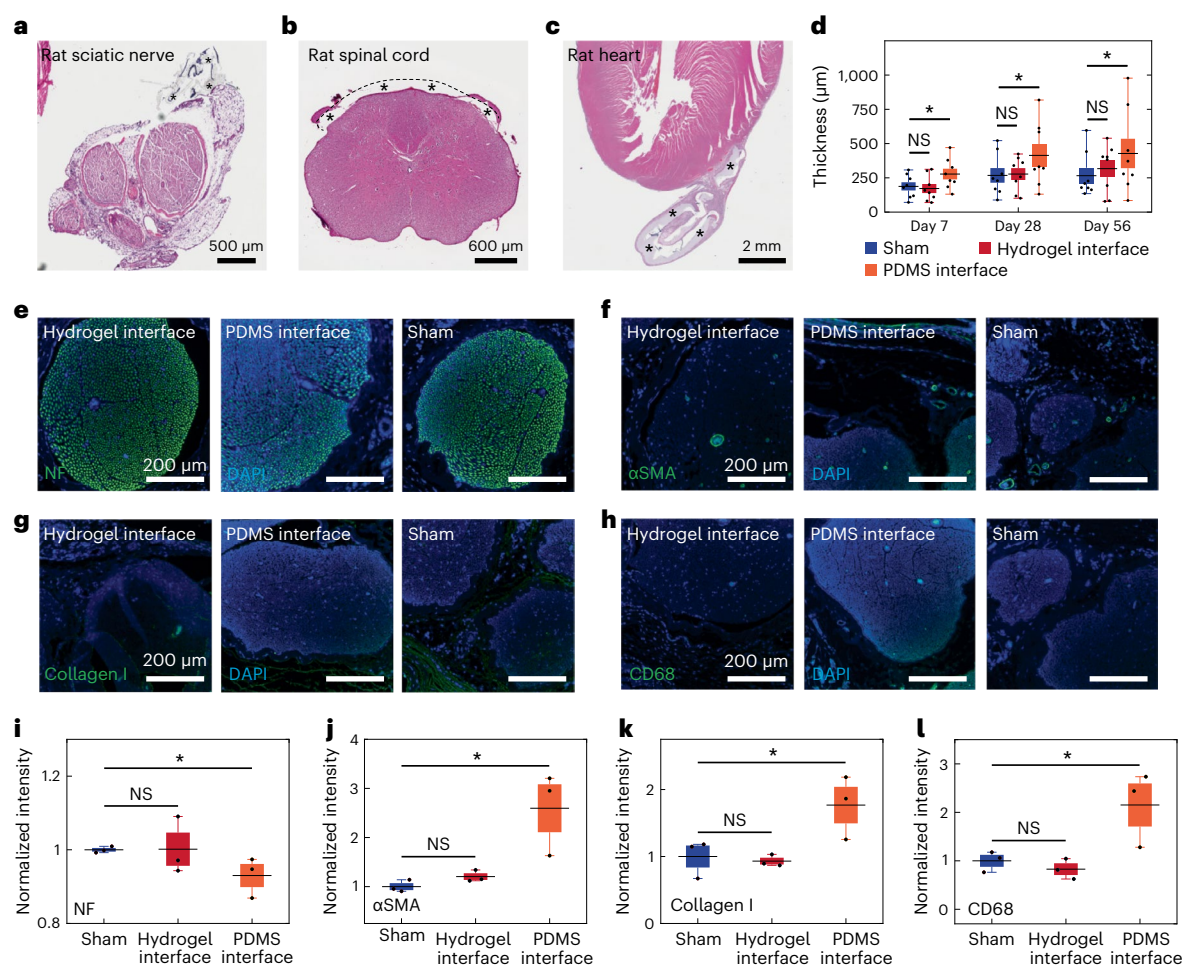
Fig. 6 | In vivo biocompatibility. a–c, Representative histological images of rat sciatic nerve (**a**), spinal cord (**b**) and heart (**c**) stained with haematoxylin and eosin on day 28 post-implantation of the all-hydrogel bioelectronic interfaces. Each experiment was repeated independently 3 times. An asterisk indicates the implanted hydrogel bioelectronic interface. **d**, Sciatic nerve epineurium thickness measured from histological images on day 7, day 28 and day 56 post-implantation of the all-hydrogel bioelectronic interface, PDMS interface and sham group (no device implantation). **e–h**, Representative immunofluorescence images of rat sciatic nerve on day 28 post-implantation of the all-hydrogel bioelectronic interface, PDMS interface and sham group (no device implantation). Each experiment was repeated independently 3 times.

Cell nuclei are stained with DAPI (blue). Green fluorescence corresponds to the expression of neurofilament (NF, **e**), fibroblasts (αSMA, **f**), collagen (Collagen I, **g**) and macrophages (CD68, **h**), respectively. **i–l**, Normalized fluorescence intensity plots for the expression of NF (**i**), αSMA (**j**), Collagen I (**k**) and CD68 (**l**) in different groups. In box plots (**d** and **i–l**), centre lines represent mean, box limits delineate standard error, and whiskers reflect the 5th and 95th percentiles ($n = 6$ for **d**; $n = 3$ for **i–l**; independent biological replicates). Statistical significance and P values are determined by two-sided unpaired t-test; NS, not significant (in **i–l**, P values are 0.49, 0.053, 0.35 and 0.19, respectively); *$P < 0.05$ (in **i–l**, P values are 0.041, 0.016, 0.037 and 0.033, respectively).

---

systems but also for broader applications of conducting polymer hydrogels in tissue engineering and regenerative medicine[38–40].

Online content

Any methods, additional references, Nature Portfolio reporting summaries, source data, extended data, supplementary information, acknowledgements, peer review information; details of author contributions and competing interests; and statements of data and code availability are available at https://doi.org/10.1038/s41563-023-01569-2.

References

1. Yuk, H., Lu, B. & Zhao, X. Hydrogel bioelectronics. *Chem. Soc. Rev.* **48**, 1642–1667 (2019).
2. Keplinger, C. et al. Stretchable, transparent, ionic conductors. *Science* **341**, 984–987 (2013).
3. Yang, C. & Suo, Z. Hydrogel ionotronics. *Nat. Rev. Mater.* **3**, 125–142 (2018).
4. Dvir, T. et al. Nanowired three-dimensional cardiac patches. *Nat. Nanotechnol.* **6**, 720–725 (2011).
5. Ohm, Y. et al. An electrically conductive silver–polyacrylamide–alginate hydrogel composite for soft electronics. *Nat. Electron.* **4**, 185–192 (2021).
6. Tringides, C. M. et al. Viscoelastic surface electrode arrays to interface with viscoelastic tissues. *Nat. Nanotechnol.* **16**, 1019–1029 (2021).
7. Rivnay, J., Owens, Ri. M. & Malliaras, G. G. The rise of organic bioelectronics. *Chem. Mater.* **26**, 679–685 (2014).
8. Rivnay, J., Wang, H., Fenno, L., Deisseroth, K. & Malliaras, G. G. Next-generation probes, particles, and proteins for neural interfacing. *Sci. Adv.* **3**, e1601649 (2017).
9. Gong, J. P., Katsuyama, Y., Kurokawa, T. & Osada, Y. Double-network hydrogels with extremely high mechanical strength. *Adv. Mater.* **15**, 1155–1158 (2003).

10. Sun, J.-Y. et al. Highly stretchable and tough hydrogels. *Nature* **489**, 133–136 (2012).

11. Hua, M. et al. Strong tough hydrogels via the synergy of freeze-casting and salting out. *Nature* **590**, 594–599 (2021).

12. Liu, C. et al. Tough hydrogels with rapid self-reinforcement. *Science* **372**, 1078–1081 (2021).

13. Zhao, X. et al. Soft materials by design: unconventional polymer networks give extreme properties. *Chem. Rev.* **121**, 4309–4372 (2021).

14. Dai, T. et al. Mechanically strong conducting hydrogels with special double-network structure. *Synth. Met.* **160**, 791–796 (2010).

15. Naficy, S., Oveissi, F., Patrick, B., Schindeler, A. & Dehghani, F. Printed, flexible pH sensor hydrogels for wet environments. *Adv. Mater. Technol.* **3**, 1800137 (2018).

16. Zhao, Y. et al. Hierarchically structured stretchable conductive hydrogels for high-performance wearable strain sensors and supercapacitors. *Matter* **3**, 1196–1210 (2020).

17. Wei, H. et al. Orthogonal photochemistry-assisted printing of 3D tough and stretchable conductive hydrogels. *Nat. Commun.* **12**, 2082 (2021).

18. Javadi, M. et al. Conductive tough hydrogel for bioapplications. *Macromol. Biosci.* **18**, 1700270 (2018).

19. Yao, B. et al. Ultrahigh-conductivity polymer hydrogels with arbitrary structures. *Adv. Mater.* **29**, 1700974 (2017).

20. Liu, Y. et al. Soft and elastic hydrogel-based microelectronics for localized low-voltage neuromodulation. *Nat. Biomed. Eng.* **3**, 58–68 (2019).

21. Lu, B. et al. Pure PEDOT: PSS hydrogels. *Nat. Commun.* **10**, 1043 (2019).

22. Liu, Y. et al. Morphing electronics enable neuromodulation in growing tissue. *Nat. Biotechnol.* **38**, 1031–1036 (2020).

23. Zhao, X. Multi-scale multi-mechanism design of tough hydrogels: building dissipation into stretchy networks. *Soft Matter* **10**, 672–687 (2014).

24. Feig, V. R., Tran, H., Lee, M. & Bao, Z. Mechanically tunable conductive interpenetrating network hydrogels that mimic the elastic moduli of biological tissue. *Nat. Commun.* **9**, 2740 (2018).

25. Markvicka, E. J., Bartlett, M. D., Huang, X. & Majidi, C. An autonomously electrically self-healing liquid metal–elastomer composite for robust soft-matter robotics and electronics. *Nat. Mater.* **17**, 618–624 (2018).

26. Lee, Y. Y. et al. A strain-insensitive stretchable electronic conductor: PEDOT: PSS/acrylamide organogels. *Adv. Mater.* **28**, 1636–1643 (2016).

27. Lee, S. et al. Nanomesh pressure sensor for monitoring finger manipulation without sensory interference. *Science* **370**, 966–970 (2020).

28. Qin, D., Xia, Y. & Whitesides, G. M. Soft lithography for micro- and nanoscale patterning. *Nat. Protoc.* **5**, 491–502 (2010).

29. Yuk, H. et al. 3D printing of conducting polymers. *Nat. Commun.* **11**, 1604 (2020).

30. Edelman, I. & Leibman, J. Anatomy of body water and electrolytes. *Am. J. Med.* **27**, 256–277 (1959).

31. Guimarães, C. F., Gasperini, L., Marques, A. P. & Reis, R. L. The stiffness of living tissues and its implications for tissue engineering. *Nat. Rev. Mater.* **5**, 351–370 (2020).

32. Yuk, H. et al. Dry double-sided tape for adhesion of wet tissues and devices. *Nature* **575**, 169–174 (2019).

33. Deng, J. et al. Electrical bioadhesive interface for bioelectronics. *Nat. Mater.* **20**, 229–236 (2021).

34. Yang, Q. et al. Photocurable bioresorbable adhesives as functional interfaces between flexible bioelectronic devices and soft biological tissues. *Nat. Mater.* **20**, 1559–1570 (2021).

35. Chen, X., Yuk, H., Wu, J., Nabzdyk, C. S. & Zhao, X. Instant tough bioadhesive with triggerable benign detachment. *Proc. Natl Acad. Sci.* **117**, 15497–15503 (2020).

36. Afanasenkau, D. et al. Rapid prototyping of soft bioelectronic implants for use as neuromuscular interfaces. *Nat. Biomed. Eng.* **4**, 1010–1022 (2020).

37. Park, S. et al. Adaptive and multifunctional hydrogel hybrid probes for long-term sensing and modulation of neural activity. *Nat. Commun.* **12**, 3435 (2021).

38. Guo, B. & Ma, P. X. Conducting polymers for tissue engineering. *Biomacromolecules* **19**, 1764–1782 (2018).

39. Nezakati, T., Seifalian, A., Tan, A. & Seifalian, A. M. Conductive polymers: opportunities and challenges in biomedical applications. *Chem. Rev.* **118**, 6766–6843 (2018).

40. Seo, B. R. & Mooney, D. J. Recent and future strategies of mechanotherapy for tissue regenerative rehabilitation. *ACS Biomater. Sci. Eng.* **8**, 4639–4642 (2022).

Methods

Materials

For the preparation of the BC-CPH, aqueous poly(3,4-ethylenedioxythiophene):polystyrene sulfonate (PEDOT:PSS) suspension (Clevios PH1000; Heraeus Electronic Materials), dimethyl sulfoxide (DMSO; Sigma-Aldrich), ethanol (Sigma-Aldrich) and hydrophilic polyurethane (HydroMed D3; AdvanSource Biomaterials) were used. For the preparation of the bioadhesive hydrogel ink, acrylic acid (Sigma-Aldrich), hydrophilic polyurethane (HydroMed D3; AdvanSource Biomaterials), benzophenone (Sigma-Aldrich), α-ketoglutaric acid (Sigma-Aldrich), 1-ethyl-3-(3-dimethylaminopropyl) carbodiimide (Sigma-Aldrich) and N-hydroxysuccinimide (NHS; Sigma-Aldrich) were used. For the preparation of the on-demand detachable bioadhesive hydrogel ink, NHS ester functionalized monomer with disulfide bond was synthesized following the previously reported protocol[35]. For the preparation of the insulating hydrogel ink, low water content hydrophilic polyurethane (HydroThane AL-25 80A, AdvanSource Biomaterials), dimethylformamide (Sigma-Aldrich) and tetrahydrofuran (Sigma-Aldrich) were used. For the preparation of fluorescent hydrophilic polyurethane, fluorescein o-acrylate (Sigma-Aldrich) was used. For printing of the all-hydrogel bioelectronic interfaces, poly(vinyl alcohol) (PVA; molecular weight (Mw) 31,000–50,000, 87–89% hydrolysed, Sigma-Aldrich), 100 μm and 200 μm nozzles (Nordson EFD) and 5 ml syringe barrel (Nordson EFD) were used. All animal studies in this work were reviewed and approved by the Committee on Animal Care at the Massachusetts Institute of Technology (MIT).

Preparation of the BC-CPH

An aqueous PEDOT:PSS suspension was stirred vigorously for 6 h at room temperature and filtered with a syringe filter (0.45 μm polypropylene). The filtered PEDOT:PSS suspension was transferred to a clean glass vial and cryogenically frozen by submerging in a liquid nitrogen bath. The cryogenically frozen PEDOT:PSS suspension was lyophilized for 72 h to isolate PEDOT:PSS nanofibrils. The isolated PEDOT:PSS nanofibrils were re-dispersed with de-ionized water and DMSO mixture (water:DMSO = 85:15 v/v) at the concentration of 7 w/w%, followed by thorough mixing and homogenization by a mortar grinder (RM 200; Retch). The re-dispersed PEDOT:PSS suspension was then mixed with 7 w/w% hydrophilic polyurethane in ethanol solution (ethanol:de-ionized water = 95:5 v/v) at varying ratio. The mixture was further diluted with the mixed solvent (70 v/v% ethanol and 30 v/v% water) to prepare a high-viscosity printable BC-CPH ink (7 w/w% polymer concentration) or a low-viscosity spin-coatable BC-CPH ink (0.5 w/w% polymer concentration), followed by filtering with a syringe filter (10 μm polypropylene). The BC-CPH was prepared by air drying the BC-CPH ink at room temperature for 24 h to minimize the formation of air bubbles from rapid evaporation of solvent (Supplementary Fig. 33). The dried sample was swollen in a large volume of PBS before use. Otherwise mentioned, the BC-CPH with 25 w/w% PEDOT:PSS concentration (PEDOT:PSS: hydrophilic polyurethane = 1:3 w/w) was used.

Preparation of the bioadhesive hydrogel ink

To prepare a precursor solution, add 32 w/w% acrylic acid, 8 w/w% hydrophilic polyurethane, 1.1 w/w% benzophenone and 0.1 w/w% α-ketoglutaric acid in ethanol solution (ethanol:de-ionized water = 2:1 v/v). To graft polyacrylic acid to the hydrophilic polyurethane (PU-PAA), the homogeneously mixed precursor solution was transferred to a sealed glass vial and cured in an ultraviolet (UV) crosslinker (365 nm, 15 W powder) for 120 min. For the preparation of the on-demand detachable bioadhesive hydrogel ink, 1 w/w% NHS ester functionalized monomer with disulfide bond was added before UV curing. The cured precursor solution was then purified by using cellulose dialysis bags in a pure ethanol bath for 24 h (bath replaced every 12 h) followed by in a de-ionized water bath for 24 h (bath replaced every 12 h) with continuous magnetic stirring. The purified PU-PAA samples were cut into small pieces and thoroughly dried in a vacuum desiccator for 24 h. To prepare the bioadhesive hydrogel ink, the dried PU-PAA was dissolved in 70% ethanol solution at a concentration of 20 w/w%. About 2 w/w% 1-ethyl-3-(3-dimethylaminopropyl) carbodiimide and 2 w/w% NHS were added to the bioadhesive hydrogel ink before printing to introduce NHS ester groups to PU-PAA (this step was skipped for the on-demand detachable bioadhesive hydrogel ink). The bioadhesive was prepared by air drying the printed ink at room temperature for 24 h and used in the dry state to facilitate wet adhesion. To prepare the bioadhesive hydrogel in mechanical characterizations, the dry bioadhesive sample was swollen in a large volume of PBS.

Preparation of the insulating hydrogel ink

To prepare the insulating hydrogel ink, low water content hydrophilic polyurethane was dissolved in a solvent mixture (dimethylformamide: tetrahydrofuran = 1:1 v/v) at a concentration of 25 w/w%. The insulating hydrogel was prepared by air drying the printed ink at 70 °C for 3 h and swelling the dried sample in a large volume of PBS.

Preparation of conducting polymer hydrogels based on hydrophilic polymer matrix

Aqueous solutions of polyvinyl alcohol, polyacrylamide or polyacrylic acid were prepared by dissolving 7 w/w% polymer in de-ionized water. The polymer solution was then mixed with the re-dispersed 7 w/w% PEDOT:PSS suspension at a 1:1 volume ratio, followed by filtering with a syringe filter (10 μm polypropylene). Conducting polymer hydrogels were prepared by air drying the precursor solution at 60 °C for 2 h followed by annealing at 90 °C for 30 min and swelling the dry-annealed sample in a large volume of PBS.

Mechanical characterizations

All mechanical characterizations were performed by using the fully swollen samples in PBS. Mechanical properties of the samples were characterized by a mechanical testing machine (U-Stretch with 4.4 N load cell; CellScale). All mechanical characterizations were performed within the submersion stage filled with PBS to avoid dehydration of the sample at a constant crosshead speed of 50 mm min^{-1}. No statistical methods were used to pre-determine sample sizes, but our sample sizes are similar to those reported in previous publications.[36,29]

For measurement of ultimate strain and Young's modulus, dog-bone samples (10 mm in gauge length, 3 mm in width, 0.2 mm in thickness) were used. The ultimate strain of the sample was measured based on the engineering strain at which the sample ruptured. Young's modulus of the sample was measured by fitting the engineering stress versus engineering strain curve with the incompressible neo-Hookean model for uniaxial extension,

$$S = \frac{E}{3}\left(\varepsilon + 1 - \frac{1}{(\varepsilon + 1)^2}\right) \tag{1}$$

where S is the engineering stress, E is the Young's modulus of the sample and ε is the engineering strain.

For measurement of fracture toughness, rectangular samples (20 mm in length, 40 mm in width, 0.2 mm in thickness) without or with notch (10 mm in length) were used. The fracture toughness of the sample was calculated by following the previously reported method based on tensile tests of unnotched and notched samples[10].

For measurement of interfacial toughness, dry bioadhesives (30 mm in length, 10 mm in width, 0.2 mm in thickness) adhered to various tissues (sciatic nerve, spinal cord, heart, muscle) were tested by the 180° peel test[32]. The measured force reached a plateau as the peeling process entered the steady state. Interfacial toughness was determined by dividing two times the plateau force by the width of the sample. Poly(methyl methacrylate) films (with a thickness of 50 μm; Goodfellow) were applied using cyanoacrylate glue (Krazy Glue) as a stiff backing for

the tissues and hydrogels. All rat tissues used for the measurement of interfacial toughness were collected and used following the protocol reviewed and approved by the Committee on Animal Care at MIT.

Rheological characterizations of the various inks were conducted by using a rotational rheometer (AR-G2; TA Instrument) with 20-mm-diameter steel parallel-plate geometry. Viscosity was measured as a function of shear rate by steady-state flow tests with a logarithmic sweep of shear rate ($0.01\,s^{-1}$ to $1,000\,s^{-1}$). All rheological characterizations were conducted at 25 °C with a preliminary equilibration time of 1 min.

Electrical characterizations

For electrical characterizations, the free-standing BC-CPH films (30 mm in length, 5 mm in width, 0.1 mm in thickness) or the all-hydrogel bioelectronic interface for sciatic nerve fully swollen in PBS were used. The electrical conductivity of the sample was measured by using a standard four-point probe (Keithley 2700; Keithley). Pt wire electrodes (0.5 mm in diameter) were attached to the surface of the sample by applying the silver paste. The electrical conductivity of the samples was calculated as

$$\sigma = \frac{I \times L}{V \times W \times T} \tag{2}$$

where σ is the electrical conductivity, I is the current flowing through the sample, L is the distance between the two electrodes for voltage measurement, V is the voltage across the electrodes, W is the width of the sample, and T is the thickness of the sample.

Electrochemical impedance spectroscopy measurements of the sample were performed by using a potentiostat/galvanostat (1287A, Solartron Analytical) and a frequency response analyser (1260A, Solartron Analytical) in an electrochemical cell installed with the sample as a working electrode, a Pt sheet as a counter electrode, an Ag/AgCl wire as a reference electrode and PBS as an electrolyte. The frequency range between 0.1 kHz and 100 kHz was scanned with an applied bias of 0.01 V versus Ag/AgCl.

Cyclic voltammetry measurements were performed by using a potentiostat/galvanostat (VersaSTAT 3; Princeton Applied Research) with the potential window of ±0.5 V versus Ag/AgCl and a potential scan rate of $150\,mV\,s^{-1}$ in an electrochemical cell installed with the sample as a working electrode, a Pt sheet as a counter electrode, an Ag/AgCl wire as a reference electrode and PBS as an electrolyte. The CSC of the sample was calculated from the measured cyclic voltammetry data as

$$CSC = \int_{E_2}^{E_1} \frac{i(E)}{2vA} dE \tag{3}$$

where v is the scan rate, E_2 and E_1 are the potential window, i is the current at each potential and A is the area of the sample.

To measure charge injection capacity (CIC), biphasic pulses at 200 ms with the amplitude ±0.5 V were applied by using a multi-channel potentiostat (VMP3, Bio-Logic Science Instruments) in an electrochemical cell installed with the sample as a working electrode, a Pt sheet as a counter electrode, an Ag/AgCl wire as a reference electrode and PBS as an electrolyte. The CIC of the sample was calculated from the measured output voltage and current as

$$CIC = \frac{Q_{inj(c)} + Q_{inj(a)}}{A} \tag{4}$$

where $Q_{inj(c)}$ is the total delivered (or injected) charge in the cathodal phase, $Q_{inj(a)}$ is the total delivered (or injected) charge in the anodal phase and A is the area of the sample.

Atomic force microscope phase imaging

Atomic force microscope (AFM) phase images were acquired by an AFM (MFP-3D, Asylum Research). Undeformed or stretched free-standing BC-CPH films were directly attached to the sample stage by double-sided carbon tape.

Energy-dispersive X-ray spectroscopy

Zeiss Merlin scanning electron microscope (SEM) with energy-dispersive X-ray spectroscopy was used for elemental analysis. Energy-dispersive X-ray spectroscopy data were acquired at 15 kV.

Micro-moulding by soft lithography

A 3-inch silicon wafer (University Wafer) was cleaned by oxygen plasma (50 W) for 1 min. Photoresist SU-8 (SU-8 2010; MicroChem) was spin-coated on the wafer at 2,000 rpm for 1 min, followed by pre-baking sequentially at 60 °C for 1 min and 95 °C for 4 min. The photoresist was then patterned by photolithography with a mask aligner (SUSS MA6 Mask Aligner; SUSS MicroTec). After the photolithography exposure, the silicon wafer was post-baked sequentially at 65 °C for 1 min and 95 °C for 4 min. The SU-8 photoresist was developed (SU-8 Developer; Micro-Chem) for 1.5 min, followed by rinsing with isopropanol and drying with nitrogen gas. The high-viscosity BC-CPH ink was applied on the prepared mould, dried for 30 min at 40 °C and peeled off from the substrate.

Printing of the all-hydrogel bioelectronic interfaces

Before the printing of the all-hydrogel bioelectronic interfaces, a layer of PVA was introduced as a water-dissolvable substrate for the hydrogel interface. To introduce the PVA layer, an aqueous PVA solution (30 $w/w\%$ in de-ionized water) was spin-coated on a printing substrate at 600 rpm for 1 min followed by drying at 70 °C for 1 h. Multi-material printing was conducted by a custom-designed 3D printer based on a Cartesian gantry system (AGS1000; Aerotech) with various sizes of nozzles (200 μm and 100 μm nozzles) connected to syringe barrels loaded with the BC-CPH, bioadhesive and insulating hydrogel inks[29]. Printing paths were prepared by computer-aided design drawings (SolidWorks; Dassault Systèmes) and converted into G-codes by a commercial software package (CADFusion (version 2.05); Aerotech) to command the x-y-z motion of the printer head. The all-hydrogel bioelectronic interfaces for animal studies were prepared in an aseptic manner and were further disinfected under UV light for 15 min.

Biodegradation characterizations

Storage medium was prepared by adding 5 mg collagenase and 5 mg lysozyme in 100 ml Dulbecco's PBS[32]. The BC-CPH or all-hydrogel bioelectronic interfaces were stored in the storage medium at 37 °C. During the storage duration, cathode-first charge-balanced electrical pulses (1 Hz, 0.5 mA) with a width of 0.2 ms were applied by the RHS Stim/Recording Controller to the all-hydrogel bioelectronic interfaces daily for 1 h.

In vitro cytotoxicity characterizations

In vitro cytotoxicity characterizations were performed by using the BC-CPH, bioadhesive hydrogel, insulating hydrogel and all-hydrogel bioelectronic interface conditioned media for cell culture. To prepare the conditioned media for each material, 20 mg of sample was incubated in 1 ml Dulbecco's modified eagle medium supplemented with 10 $v/v\%$ FBS and 100 U ml^{-1} penicillin–streptomycin at 37 °C for 24 h. The supplemented Dulbecco's modified eagle medium without incubating sample was used as a control group. Rat embryonic cardiomyocytes (H9c2(2-1), ATCC) were added in a confocal dish (20 mm diameter) at a density of 0.5×10^5 cells ($n = 4$ per each group). The cells were treated with the conditioned or control media and incubated at 37 °C for 24 h in 5% CO_2. The cell viability was determined by a LIVE/DEAD viability/cytotoxicity kit for mammalian cells (Thermo Fisher Scientific). A laser confocal microscope (SP 8, Leica) was used to image live cells with excitation/emission at 495 nm/515 nm and dead cells at 495 nm/635 nm, respectively. The cell viability was calculated by counting the number of live (green fluorescence) and dead (red fluorescence) cells by using ImageJ (version 2.1.0).

Vertebrate animal subjects

Female Sprague Dawley rats (225–250 g, 12 weeks, Charles River) were used in this work. Animals were randomly assigned to the various experimental groups. All animal studies were reviewed and approved by the Committee on Animal Care at MIT. The animal care and use programs at MIT meet the requirements of the Federal Law (89-544 and 91-579) and NIH regulations and are also accredited by the American Association for Accreditation of Laboratory Animal Care.

In vivo sciatic nerve surgeries

Animals were anaesthetized using 3% inhaled isoflurane. Animals were placed in the prone position over a heating pad for the duration of the surgery. Anaesthesia was maintained with a nose cone and 1–2% isoflurane in O_2. Respiratory rate and quality were used to monitor the depth of anaesthesia. Sterile eye ointment was applied after anaesthesia and before shaving to minimize the risk of corneal irritation, dehydration and sensitization during surgical procedures. Before starting the surgery, the depth of anaesthesia was checked by monitoring of tail and toe pinch response. The surgical sites of the animals were shaved to remove dorsocaudal region hair, and the shaved area was prepared with an application of Betadine and three subsequent applications of 70% ethanol rinses, each with a contact time of at least 2 min. A 2 cm incision was made through the dermis of the animal's hindlimb, exposing the subcutaneous tissue. The sciatic nerve was exposed by separating the muscles close to the femur. The all-hydrogel bioelectronic interface ($n = 3$ for day 7, $n = 3$ for day 28, $n = 3$ for day 56) or the PDMS interface (control, $n = 3$ for day 7, $n = 3$ for day 28, $n = 3$ for day 56) were implanted on the surface of the exposed sciatic nerve. For the sham group ($n = 3$ for day 7, $n = 3$ for day 28, $n = 3$ for day 56), no device was implanted. Two samples were implanted per animal for both right and left hindlimbs. The incision was closed with 4–0 sutures, and 3–6 ml of warm saline was injected subcutaneously as post-surgical hydration support. The all-hydrogel bioelectronic interfaces were fully functional during the study period, and the study endpoints were determined for investigational purposes and not by failure of the implants. All animals in the study survived and were kept in normal health conditions based on daily monitoring by the MIT Division of Comparative Medicine (DCM) veterinarian staff.

In vivo spinal cord surgeries

Animals were anaesthetized using 3% inhaled isoflurane. Animals were placed in the prone position over a heating pad for the duration of the surgery. Anaesthesia was maintained with a nose cone and 1–2% isoflurane in O_2. Respiratory rate and quality were used to monitor the depth of anaesthesia. Sterile eye ointment was applied after anaesthesia and before shaving to minimize the risk of corneal irritation, dehydration and sensitization during surgical procedures. Before starting the surgery, the depth of anaesthesia was checked by monitoring of tail and toe pinch response. The surgical site of the animals was shaved to remove the hair from slightly rostral to the ears to the middle of the animal's back. The shaved area was prepared with an application of Betadine and three subsequent applications of 70% ethanol rinses, each with a contact time of at least 2 min. A small incision around 10 mm in length above the vertebrae of interest (C4–C6) was created by using a scalpel blade. The size of the opening in the skin was then increased by blunt dissection with forceps or surgical scissors. Further incisions were made through the muscle layers over the spinal column using a scalpel blade. The surgical field was made by retracing the muscle tissues by using a sterile autoclaved soft tissue retractor. All overlying tissues from the dorsal laminae were removed by using a spring scissor and sterile cotton swabs, and the spinal column was secured with rat-toothed forceps. A laminectomy was conducted by grabbing the entire lamina with a rongeur and slowly breaking the lamina with a rongeur or spring scissors. The broken pieces of the spine were gently pulled upwards, and the surrounding connective tissues were cleaned off to expose the spinal cord. The all-hydrogel bioelectronic interface

($n = 3$) was implanted on the spinal cord epidurally from the entry point with the help of a sterilized thin polyethylene terephthalate film (100 μm thick, Goodfellow). For the sham group ($n = 3$), no device was implanted. The incision was closed with 4–0 sutures, and 3–6 ml of warm saline was injected subcutaneously as post-surgical hydration support. The all-hydrogel bioelectronic interfaces were fully functional during the study period, and the study endpoints were determined for investigational purposes and not by failure of the implants. All animals in the study survived and were kept in normal health conditions based on daily monitoring by the MIT DCM veterinarian staff.

In vivo heart surgeries

Animals were anaesthetized using 3% inhaled isoflurane. Anaesthesia was maintained with a nose cone and 1–2% isoflurane in O_2. Respiratory rate and quality were used to monitor the depth of anaesthesia. Sterile eye ointment was applied after anaesthesia and before shaving to minimize the risk of corneal irritation, dehydration and sensitization during surgical procedures. Before starting the surgery, the depth of anaesthesia was checked by monitoring of tail and toe pinch response. Chest hair was then removed. Endotracheal intubation was performed, and the animals were connected to a mechanical ventilator (RoVent, Kent Scientific) and placed supine over a heating pad for the duration of the surgery. The shaved area was prepared with an application of Betadine and three subsequent applications of 70% ethanol rinses, each with a contact time of at least 2 min. The heart was exposed via a thoracotomy in the third or fourth left intercostal space, and the pericardium was removed with fine forceps. The all-hydrogel bioelectronic interface ($n = 3$) was implanted on the epicardium of the exposed heart. For the sham group ($n = 3$), no device was implanted. The incision was closed with 4–0 sutures, and 3–6 ml of warm saline was injected subcutaneously as post-surgical hydration support. The animals were ventilated with 100% oxygen until autonomous breathing was regained, and the intubation catheter was removed. The all-hydrogel bioelectronic interfaces were fully functional during the study period, and the study endpoints were determined for investigational purposes and not by failure of the implants. All animals in the study survived and were kept in normal health conditions based on daily monitoring by the MIT DCM veterinarian staff.

In vivo sciatic nerve stimulation

On day 0, day 7, day 28 and day 56 post-implantation, the implanted animals were anaesthetized by using inhaled isoflurane. The input and output end of the implanted all-hydrogel bioelectronic interface was connected to a RHS Stim/Recording Controller (Intan Technologies) through a custom-designed printed circuit board (PCB) with a flat flexible cable (Digi-Key Electronics). A needle electrode was inserted into the skin of the other hindlimb as the reference and ground. Cathode-first charge-balanced electrical pulses (1 Hz, 0.2–1 mA) with a width of 0.2 ms were applied by the RHS Stim/Recording Controller. A protractor marker was placed under the animal's hindlimb to measure the change in the angle of the ankle joint. A Pt electrode (A-M Systems) was inserted into the desired muscles for electromyogram (EMG) recordings through the RHS Stim/Recording Controller and RHS amplifier (Intan Technologies) at a sampling rate of 20 kHz.

In vivo spinal cord stimulation

On day 0, day 7 and day 28 post-implantation, the implanted animals were anaesthetized by using inhaled isoflurane. The animals were placed on a custom-made body supporter to allow the forelimbs to move freely. The input and output end of the implanted all-hydrogel bioelectronic interface was connected to the RHS Stim/Recording Controller through the custom-designed PCB with the flat flexible cable. A needle electrode was inserted into the skin on the back as the reference and ground. Cathode-first charge-balanced electrical pulses (1 Hz, 0.3–2.5 mA) with a width of 0.2 ms were applied by the RHS Stim/Recording Controller. A ruler was placed between the animal's forelimb

and the custom-made body supporter to measure the movement distance of the animal's forelimbs. A Pt electrode was inserted into the desired muscles for EMG recordings through the RHS Stim/Recording Controller and RHS amplifier at a sampling rate of 20 kHz.

In vivo epicardial recording

On day 0, day 7 and day 28 post-implantation, the implanted animals were anaesthetized by using inhaled isoflurane. The input and output end of the implanted all-hydrogel bioelectronic interface was connected to the RHS Stim/Recording Controller through the custom-designed PCB with the flat flexible cable. A needle electrode was inserted into the left forelimb as the reference and ground. Epicardial signals were then collected with the RHS Stim/Recording Controller and RHS amplifier at a sampling rate of 20 kHz. The SNR was calculated by dividing the average peak-to-peak amplitude of recorded signals by noise derived from noise estimation of corresponding recording traces.

In vivo on-demand detachment

A detachment solution was prepared by dissolving 0.5 M sodium bicarbonate and 50 mM L-glutathione reduced in PBS[35]. To remove the adhered all-hydrogel bioelectronic interface on demand, 1–2 ml of the detachment solution was applied to the adhered hydrogel bioadhesive. After 5 min, the applied detachment solution was removed by a sterile gauze, and the all-hydrogel bioelectronic interface was gently removed by pulling with a forceps.

Histology

At the end of each study, the animals were euthanized by CO_2 inhalation. The tissue of interest was excised and fixed in 10% formalin solution for 24 h for histological processing. The fixed tissue samples were placed in 70% ethanol and submitted for paraffin embedding, sectioning and haematoxylin–eosin staining at the Hope Babette Tang (1983) Histology Facility in the Koch Institute for Integrative Cancer Research at MIT. The completed histology slides were scanned by using a digital slide scanner (Aperio, Leica). All histological assessments were conducted by the blinded pathologist based on randomly mixed histological slides without informing the type or study group of samples. No data were excluded.

Immunofluorescence analysis

For immunofluorescence analysis, the sectioned slides were deparaffinized and rehydrated in de-ionized water. Antigen retrieval was performed using a steam method during which the slides were steamed in IHC-Tek Epitope Retrieval Solution (IW-1100) for 35 min and then cooled for 20 min. Then the slides were washed in three changes of PBS for 5 min per cycle. After washing, the slides were incubated in primary antibodies (1:1,000 rabbit anti-neurofilament for neurofilament (ab8135, Abcam); 1:200 mouse anti-α-SMA for fibroblast (ab7817, Abcam); 1:200 mouse anti-CD68 for macrophages (ab201340, Abcam); 1:200 rabbit anti-collagen-I for collagen (ab21286, Abcam); 1:100 rabbit anti-CD3 for T cells (ab5690, Abcam)) diluted with IHC-Tek Antibody Diluent for 1 h at room temperature. The slides were then washed three times in PBS and incubated with Alexa Fluor 488 labelled anti-rabbit or anti-mouse secondary antibody (1:400, Jackson Immunoresearch) for 30 min. The slides were washed in PBS and then counterstained with DAPI for 20 min. A laser confocal microscope (SP 8, Leica) was used for image acquisition. MATLAB (version R2018b) was used to quantify the fluorescence intensity of expressed antibodies. Blue channel was DAPI staining for nucleus and thus not included in quantitative analysis. Only green channel was for specifically stained antibodies and thus included in quantitative analysis. All the images for analysing were transformed into double-precision images for analysis. Fluorescence intensities were calculated and normalized against the mean values of the corresponding sham groups. All analyses were blinded with respect to the experimental conditions.

Statistical analysis

Prism 9 (GraphPad, version 9.1) software was used to assess the statistical significance of all comparison studies in this work. Data distribution was assumed to be normal for all parametric tests but not formally tested. In the statistical analysis for comparison between multiple samples, one-way ANOVA followed by Bonferroni's multiple comparison test was conducted with the threshold of $*P < 0.05$, $**P \leq 0.01$ and $***P \leq 0.001$. In the statistical analysis between two data groups, two-sided unpaired t-test was used with the threshold of $*P < 0.05$, $**P \leq 0.01$ and $***P \leq 0.001$.

Reporting summary

Further information on research design is available in the Nature Portfolio Reporting Summary linked to this article.

Data availability

All data supporting the findings of this study are available within the Article and its Supplementary Information. Additional raw data generated in this study are available from the corresponding authors on reasonable request.

Author contributions

H.Y., B.L. and X.Z. developed the concept and materials for the BC-CPH. H.Y. and T.Z. developed the materials and method for the printing-based fabrication and application of the all-hydrogel bioelectronic interfaces. B.L., H.Y., F.H., F.T. and J.X. conducted the electrical and mechanical characterizations of the BC-CPH. T.Z. and H.Y. conducted the electrical and mechanical characterizations of the all-hydrogel bioelectronic interfaces. T.Z., H.Y. and J.W. designed and conducted the in vivo animal studies. H.Y. and H.R. developed the materials and method for the printable bioadhesive. Z.S. and G.G. conducted the AFM phase imaging. H.Y. and X.Z. developed the multi-material printing platform. H.Y. prepared figures with inputs from all authors. H.Y., T.Z. and X.Z. wrote the manuscript with inputs from all authors.

Competing interests

H.Y. and X.Z. have a financial interest in SanaHeal, a biotechnology company focused on the development of medical devices for surgical sealing and repair. The other authors declare no competing interests.
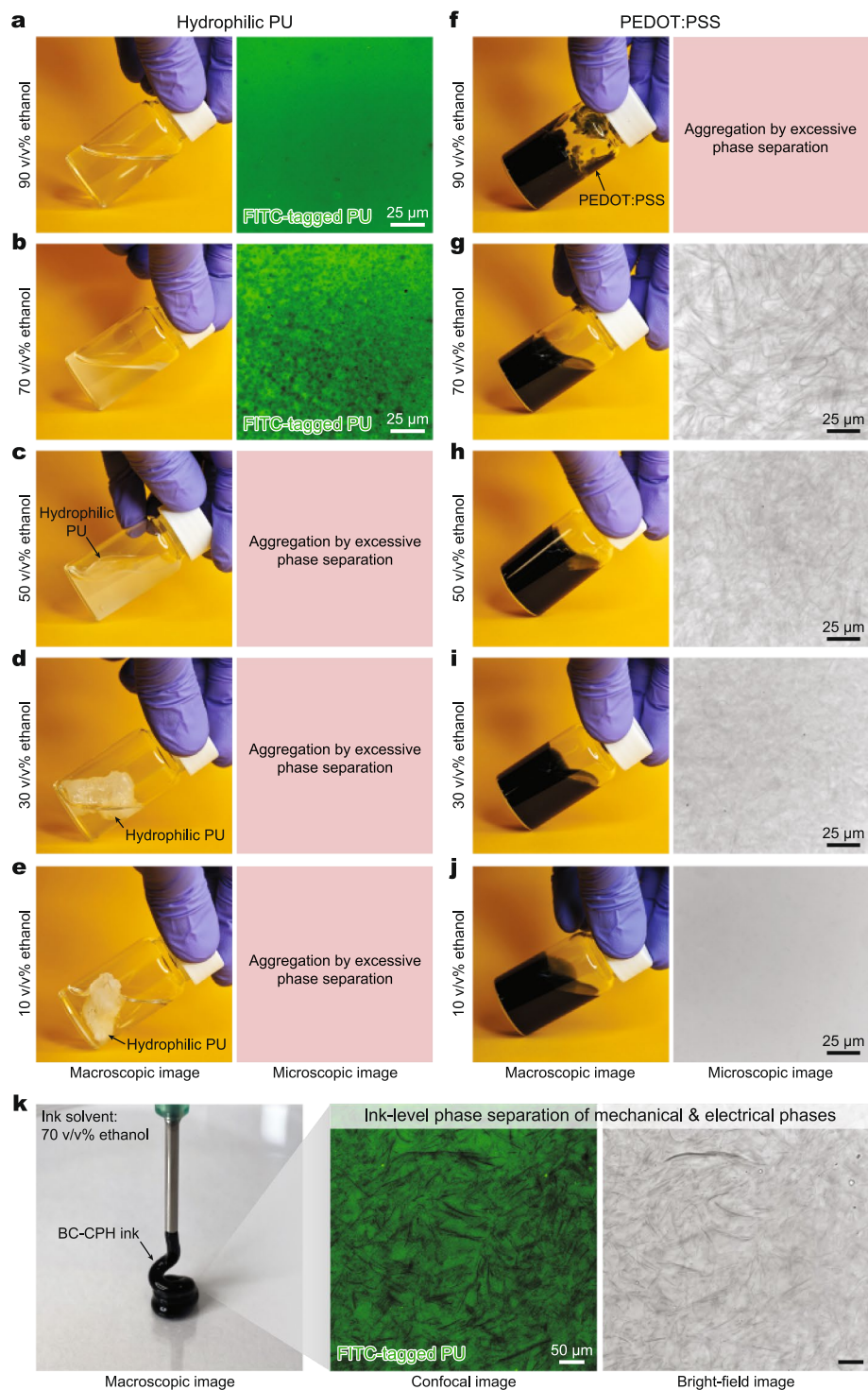
Additional information

Extended data is available for this paper at https://doi.org/10.1038/s41563-023-01569-2.

Supplementary information The online version contains supplementary material available at https://doi.org/10.1038/s41563-023-01569-2.

Correspondence and requests for materials should be addressed to Hyunwoo Yuk, Baoyang Lu or Xuanhe Zhao.

Peer review information Nature Materials thanks Tal Dvir and the other, anonymous, reviewer(s) for their contribution to the peer review of this work.

**Reprints and permissions information** is available at www.nature.com/reprints.

a Hydrophilic PU
f PEDOT:PSS

90 v/v% ethanol
70 v/v% ethanol
50 v/v% ethanol
30 v/v% ethanol
10 v/v% ethanol

FITC-tagged PU — 25 µm
FITC-tagged PU — 25 µm
Aggregation by excessive phase separation
Aggregation by excessive phase separation
Aggregation by excessive phase separation

Hydrophilic PU
Hydrophilic PU
Hydrophilic PU

PEDOT:PSS
Aggregation by excessive phase separation

Macroscopic image — Microscopic image

k Ink solvent: 70 v/v% ethanol

BC-CPH ink

Ink-level phase separation of mechanical & electrical phases

FITC-tagged PU — 50 µm

Macroscopic image — Confocal image — Bright-field image

Extended Data Fig. 1 | Phase-separation of electrical and mechanical phases in the BC-CPH ink. a–e, Macroscopic (left) and microscopic (right) images of hydrophilic polyurethane (PU) dissolved in ethanol-water mixed solvent with 90 v/v% (a), 70 v/v% (b), 50 v/v% (c), 30 v/v% (d), and 10 v/v% (e) ethanol concentrations. Green fluorescence corresponds to PU. **f–j**, Macroscopic (left) and microscopic (right) images of PEDOT:PSS dissolved in ethanol-water mixed solvent with 90 v/v% (f), 70 v/v% (g), 50 v/v% (h), 30 v/v% (i), and 10 v/v% (j) ethanol concentration. **k**, Macroscopic (left), confocal (middle), and bright-field (right) microscopic images of the BC-CPH ink in ethanol-water mixed solvent with 70 v/v% ethanol concentration. Green fluorescence corresponds to PU. FITC, fluorescein isothiocyanate. Each experiment was repeated independently 3 times.
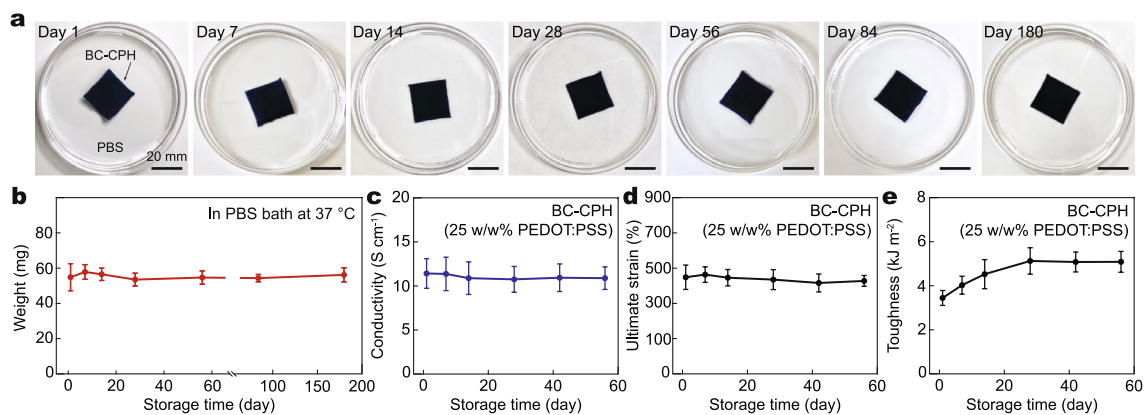
Extended Data Fig. 2 | Long-term stability of the BC-CPH in physiological environment. a,b, Images (a) and weight (b) of the BC-CPH stored in PBS at 37 °C for 1, 7, 14, 28, 56, 84, and 180 days. **c-e**, Electrical conductivity (c), ultimate strain (d), and fracture toughness (e) of the BC-CPH stored in PBS at 37 °C. Values in **b-e** represent the mean and the standard deviation (*n* = 4; independent samples).
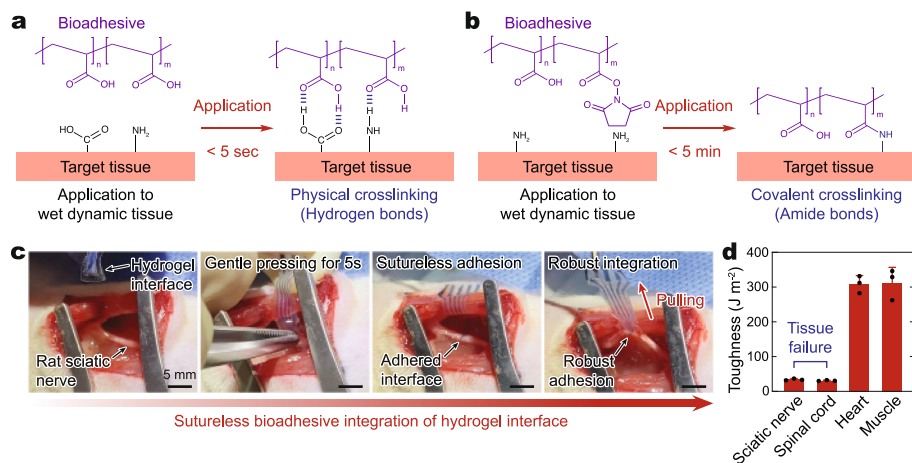
Extended Data Fig. 3 | Wet adhesion chemistry of the bioadhesive and rapid sutureless integration to wet tissues. a, Schematic illustrations for physical crosslinking between the bioadhesive and the target tissue surface by hydrogen bonds. **b**, Schematic illustrations for covalent crosslinking between the bioadhesive and the target tissue surface by amide bonds. **c**, Snapshots of sutureless bioadhesive integration of the all-hydrogel bioelectronic interface to a rat sciatic nerve. **d**, Interfacial toughness of the bioadhesive hydrogel adhered to various rat tissues. Note that tissues underwent cohesive failure for sciatic nerve and spinal cord. Values in **d** represent the mean and the standard deviation ($n = 3$; independent experiments).
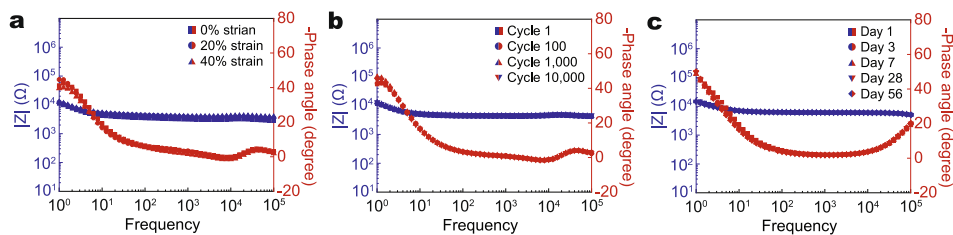
Extended Data Fig. 4 | Electrochemical stability of the all-hydrogel bioelectronic interface. a–c, Impedance (blue symbols, left axis) and phase angle (red symbols, right axis) vs. frequency plots for one electrode channel in the all-hydrogel bioelectronic interface under varying tensile strain (a), tensile cycle (b), and storage time in PBS at 37 °C (c).
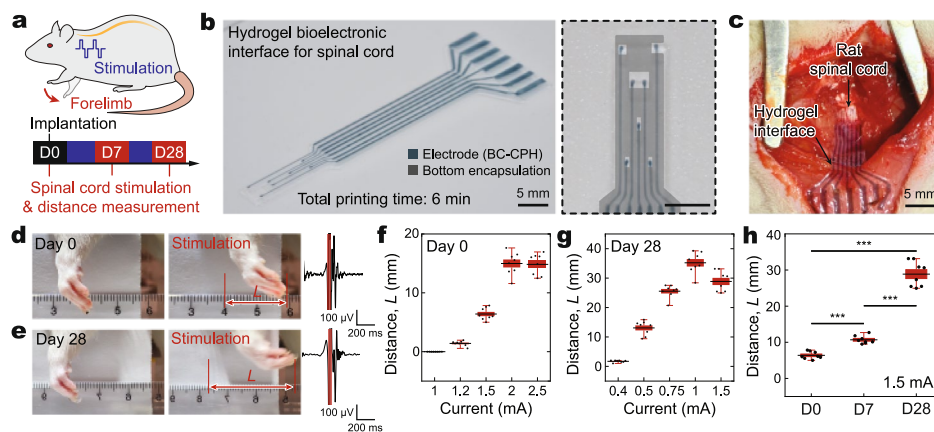
Extended Data Fig. 5 | Rat spinal cord stimulation by the all-hydrogel bioelectronic interface. a, Schematic illustration for rat spinal cord electrophysiological stimulation by the all-hydrogel bioelectronic interface. **b**, Images of the printed all-hydrogel bioelectronic interface for spinal cord in the overall view (left) and the magnified view of electrodes (right). Different materials are marked with colour overlays in the magnified view. **c**, Images of the implanted all-hydrogel bioelectronic interface on rat spinal cord. **d, e**, Images of rat forelimb before (left) and after (middle) electrophysiological stimulation of the spinal cord by the all-hydrogel bioelectronic interface with corresponding EMG recordings (right) on day 0 (d) and day 28 (e) post-implantation. The red-shaded regions in the EMG recordings indicate the stimulation pulses. **f, g**, Rat forelimb movement distance upon spinal cord stimulations by the all-hydrogel bioelectronic interface at varying stimulation currents on day 0 (f) and day 28 (g) post-implantation. **h**, Comparison of the rat forelimb movement distance on day 0, day 7, and day 28 post-implantation with stimulation current of 1.5 mA. In box plots (f-h), centre lines represent mean, box limits delineate standard error (SE), and whiskers reflect 5th and 95th percentile ($n = 8$; independent biological replicates). Statistical significance and p values are determined by two-sided unpaired t-test; *** $p \leq 0.001$.

nature research

Corresponding author(s):   Hyunwoo Yuk
Baoyang Lu
Xuanhe Zhao

Last updated by author(s): Feb 28, 2023

Reporting Summary

Nature Research wishes to improve the reproducibility of the work that we publish. This form provides structure for consistency and transparency in reporting. For further information on Nature Research policies, see our Editorial Policies and the Editorial Policy Checklist.

Statistics

For all statistical analyses, confirm that the following items are present in the figure legend, table legend, main text, or Methods section.

n/a	Confirmed	
☐	☒	The exact sample size (n) for each experimental group/condition, given as a discrete number and unit of measurement
☐	☒	A statement on whether measurements were taken from distinct samples or whether the same sample was measured repeatedly
☐	☒	The statistical test(s) used AND whether they are one- or two-sided *Only common tests should be described solely by name; describe more complex techniques in the Methods section.*
☒	☐	A description of all covariates tested
☐	☒	A description of any assumptions or corrections, such as tests of normality and adjustment for multiple comparisons
☐	☒	A full description of the statistical parameters including central tendency (e.g. means) or other basic estimates (e.g. regression coefficient) AND variation (e.g. standard deviation) or associated estimates of uncertainty (e.g. confidence intervals)
☐	☒	For null hypothesis testing, the test statistic (e.g. F, t, r) with confidence intervals, effect sizes, degrees of freedom and P value noted *Give P values as exact values whenever suitable.*
☒	☐	For Bayesian analysis, information on the choice of priors and Markov chain Monte Carlo settings
☒	☐	For hierarchical and complex designs, identification of the appropriate level for tests and full reporting of outcomes
☒	☐	Estimates of effect sizes (e.g. Cohen's d, Pearson's r), indicating how they were calculated

Our web collection on statistics for biologists contains articles on many of the points above.

Software and code

Policy information about availability of computer code

Data collection	No software used for data collection.
Data analysis	Microscopic images were analyzed by using MATLAB (Version: 2018b). All statistical analyses were performed by using Prism (Version: 7.04 GraphPad).

For manuscripts utilizing custom algorithms or software that are central to the research but not yet described in published literature, software must be made available to editors and reviewers. We strongly encourage code deposition in a community repository (e.g. GitHub). See the Nature Research guidelines for submitting code & software for further information.

Data

Policy information about availability of data

All manuscripts must include a data availability statement. This statement should provide the following information, where applicable:
- Accession codes, unique identifiers, or web links for publicly available datasets
- A list of figures that have associated raw data
- A description of any restrictions on data availability

All data supporting the findings of this study are available within the Article and its Supplementary Information. Additional raw data generated in this study are too numerous to be publicly shared, yet they are available from the corresponding authors on reasonable request.

Field-specific reporting

Please select the one below that is the best fit for your research. If you are not sure, read the appropriate sections before making your selection.

☒ Life sciences   ☐ Behavioural & social sciences   ☐ Ecological, evolutionary & environmental sciences

For a reference copy of the document with all sections, see nature.com/documents/nr-reporting-summary-flat.pdf

Life sciences study design

All studies must disclose on these points even when the disclosure is negative.

Sample size	In vivo experiments on rat were conducted to investigate in vivo biocompatibility and electrophysiological functionality. The appropriate sample size was used based on the published literatures on similar evaluations (such as Nature 575, 169-174 (2019) doi: 10.1038/s41586-019-1710-5).
Data exclusions	No data were excluded.
Replication	In vivo studies for biocompatibility and electrophysiological functionality were reliably reproduced by at least 3 times.
Randomization	All the tests were performed with randomly allocated experimental groups.
Blinding	All histological assessments were conducted by the blinded pathologist based on randomly mixed histological slides without informing type or study group of samples. Blinding was not relevant to other experiments because related experimental parameters needs to be recorded during experiments.

Reporting for specific materials, systems and methods

We require information from authors about some types of materials, experimental systems and methods used in many studies. Here, indicate whether each material, system or method listed is relevant to your study. If you are not sure if a list item applies to your research, read the appropriate section before selecting a response.

Materials & experimental systems

n/a	Involved in the study
☐	☒ Antibodies
☐	☒ Eukaryotic cell lines
☒	☐ Palaeontology and archaeology
☐	☒ Animals and other organisms
☒	☐ Human research participants
☒	☐ Clinical data
☒	☐ Dual use research of concern

Methods

n/a	Involved in the study
☒	☐ ChIP-seq
☒	☐ Flow cytometry
☒	☐ MRI-based neuroimaging

Antibodies

Antibodies used	Primary antibodies 1:1000 Rabbit anti-neurofilament for neurofilament (ab8135, Abcam); 1:200 mouse anti-α-SMA for fibroblast (ab7817, Abcam); 1:200 mouse anti-CD68 for macrophages (ab201340, Abcam); 1:200 rabbit anti-collagen-I for collagen (ab21286, Abcam); 1:100 rabbit anti-CD3 for T cells (ab5690, Abcam) Secondary antibodies Alexa Fluor 488 labeled anti-rabbit or anti-mouse secondary antibody (1:400, Jackson Immunoresearch, AB_2338046 and AB_2338840, respectively)
Validation	All antibodies are commercially available and have been tested by the manufacturer. Vendors and catalog numbers are listed above and validation can be found there. Rabbit anti-neurofilament for neurofilament (ab8135, Abcam): The antibody recognizes both phosphorylated and non-phosphorylated forms of NF-H. Specifically recognizes the heavy microfilament subunit (~180-220 kDa). Manufacturer-validated to react with Mouse, Rat (https://www.abcam.com/neurofilament-heavy-polypeptide-antibody-ab8135.html). Mouse anti-aSMA (ab7817, Abcam): This monoclonal antibody recognizes aSMA. Manufacturer-validated to react with Mouse, Rat, Rabbit, Human, Pig aSMA (https://www.abcam.com/alpha-smooth-muscle-actin-antibody-1a4-ab7817.html). Rabbit anti-Collagen I (ab21286, Abcam): This polyclonal antibody recognizes to Collagen I. Manufacturer-validated to react with Mouse, Rat Collagen I (https://www.abcam.com/collagen-i-antibody-ab21286.html).

Mouse anti-CD68 (ab201340, Abcam): This monoclonal antibody recognizes CD68. Manufacturer-validated to react with Mouse, Rat, Human CD68 (https://www.abcam.com/cd68-antibody-c68684-ab201340.html).

Rabbit anti-CD3 (ab5690, Abcam): This polyclonal antibody recognizes to CD3. Manufacturer-validated to react with Mouse, Rat, Human CD3 (https://www.abcam.com/cd3-antibody-ab5690.html).

Eukaryotic cell lines

Policy information about cell lines

Cell line source(s)	Rat embryonic cardiomyocytes (H9c2(2-1), ATCC)
Authentication	H9c2(2-1) cells from ATCC were authenticated by ATCC based on standard techniques including morphology check, isoenzyme analysis, and mycoplasma detection.
Mycoplasma contamination	Mycoplasma contamination was not detected.
Commonly misidentified lines (See ICLAC register)	No commonly misidentified cell lines were used.

Animals and other organisms

Policy information about studies involving animals; ARRIVE guidelines recommended for reporting animal research

Laboratory animals	Female Sprague Dawley rats (12 weeks, 225-275g weight) were purchased from Charles River Laboratories.
Wild animals	This study does not involve wild animals.
Field-collected samples	This study does not involve field-collected samples.
Ethics oversight	Animal procedures for rat were reviewed and approved by the Massachusetts Institute of Technology Committee on Animal Care.

Note that full information on the approval of the study protocol must also be provided in the manuscript.

3D printable high-performance conducting polymer hydrogel for all-hydrogel bioelectronic interfaces

In the format provided by the
authors and unedited

Supplementary Video Captions

Supplementary Video 1 | Multi-material 3D printing process of an all-hydrogel bioelectronic interface with the BC-CPH electrodes.

Supplementary Video 2 | Sutureless bioadhesive integration of an all-hydrogel bioelectronic interface to a rat sciatic nerve *in vivo*.

Supplementary Video 3 | On-demand detachment of an adhered all-hydrogel bioelectronic interface from a rat sciatic nerve *in vivo*.

Supplementary Discussion 1 l 3D printable bioadhesive hydrogel

The recent advances in bioadhesives have enabled rapid and sutureless adhesion to wet biological tissues and organs. For example, the dry double-sided tape (DST) and its dry-crosslinking mechanism allow the formation of robust wet adhesion to various tissues in few seconds without the need of external stimuli such as UV light[1]. Such rapid, atraumatic, and preparation-free integration to wet tissues is highly advantageous to form a stable and conformal contact between the implanted bioelectronic interface and the target tissue[1,2]. However, the existing bioadhesives are typically prepared in the form of prefabricated films that require additional assembly procedures to combine with the bioelectronic device before or during implantation *in vivo*. In this work, we developed a printable bioadhesive ink that can be readily incorporated into multi-material printing of the all-hydrogel bioelectronic interface while providing the rapid, robust, and preparation-free adhesion capability to wet tissues comparable to that of the DST.

To synergistically achieve printability, bioadhesive capability, mechanical robustness in the swollen state, and compatibility to other components of the hydrogel bioelectronic interface (i.e., the BC-CPH, the insulating hydrogel), we covalently graft a bioadhesive polymer used in the DST (PAA-NHS ester) to hydrophilic polyurethane backbones by adopting the benzophenone-based radical grafting method[3-5]. The resultant bioadhesive can be dissolved in ethanol solution at a high concentration to yield a highly viscous printable ink (Supplementary Fig. 14a) similar to the printable BC-CPH ink. The printed bioadhesive ink can be dried to provide a dry bioadhesive like the DST while forming robust mechanical integration with other components of the hydrogel bioelectronic interface (i.e., the BC-CPH, the insulating hydrogel) owing to the shared hydrophilic polyurethane-based composition of these materials.

The dry printed bioadhesive can provide rapid adhesion to wet tissues based on the dry-crosslinking mechanism[1,6]. Upon contacting the wet tissue surface, the negatively charged carboxylic acid groups in the PAA-NHS ester provide the quick hydration and swelling of the bioadhesive absorbing the interfacial water on the wet tissue surface. Simultaneously, the carboxylic acid groups in the bioadhesive physically crosslink with the tissue surface via hydrogen bonds, providing rapid initial adhesion (Extended Data Fig. 3a). Subsequently, the NHS ester groups in the bioadhesive form covalent crosslinks with primary amine groups on the tissue surface via amide bonds within few minutes from the initial adhesion, providing a stable adhesion with the target tissue (Extended Data Fig. 3b).

Taking advantage of on-demand detachment capability of the bioadhesive[7], the adhered bioadhesive can be atraumatically removed from the target tissue. Upon application of the detachment solution (0.5 M sodium bicarbonate and 50 mM L-glutathione reduced in PBS), physical crosslinks (Supplementary Fig. 15a) and covalent crosslinks (Supplementary Fig. 15b) between the bioadhesive and the tissue surface can be cleaved within 5 min. The cleavage of physical and covalent crosslinks to the tissue surface allows detachment of the bioadhesive without causing tissue damage (Supplementary Fig. 15c).

Note that other bioadhesive hydrogels that satisfy the abovementioned functionalities can be used together with the BC-CPH to construct the all-hydrogel bioelectronic interfaces.

**Supplementary Discussion 2 | 3D printable insulating hydrogel**

Hydrogels in the swollen state are ionically conductive due to the dissolved ionic species within highly-hydrated regions of the hydrogel networks[8]. Since physiological environments are wet with abundant ionic species (e.g., dissolved salts and charged biomolecules), hydrogels with high water contents typically exhibit ionic conductivity similar to that of biological tissues in physiological environments[8,9]. Hydrogels' ionic conductivity is dependent on their water contents as the ionic conductivity of hydrogels decreases with the water contents[10,11]. Notably, hydrogels with equilibrium water contents below 25-30 w/w% exhibit a substantial decrease in the ionic conductivity[12], potentially due to poor percolation between the ion-rich hydrated regions within the hydrogel[13]. Hence, we choose the low water contents hydrophilic polyurethane as an insulating hydrogel for the hydrogel bioelectronic interface. Owing to its low equilibrium water contents around 27 w/w%, the insulating hydrogel exhibits electrical insulating behavior in physiological environments (e.g., PBS) comparable to that of commonly used device encapsulating materials such as PDMS (Supplementary Fig. 16). Furthermore, the insulating hydrogel shows nearly the same electrical property in both PBS and deionized water, further confirming the electrically insulating characteristic of the hydrogel (Supplementary Fig. 17). The low water contents hydrophilic polyurethane can be dissolved in organic solvent at a high concentration to yield a highly viscous printable ink (Supplementary Fig. 14b), readily applicable to multi-material printing processes. Note that other insulating hydrogels with appropriate electrical insulation properties can be used together with the BC-CPH to construct the all-hydrogel bioelectronic interfaces.
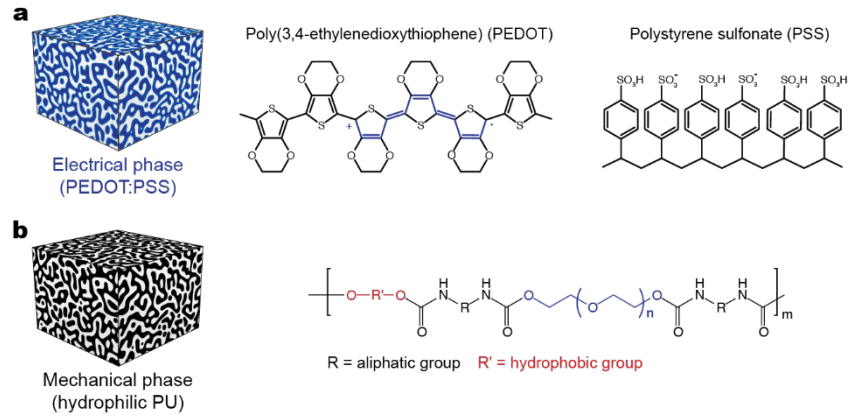
Supplementary Fig. 1 | Electrical and mechanical phases of the BC-CPH. a, Electrical phase of the BC-CPH based on poly(3,4-ethylenedioxythiophene):polystyrene sulfonate (PEDOT:PSS). **b**, Mechanical phase of the BC-CPH based on hydrophilic polyurethane (PU).
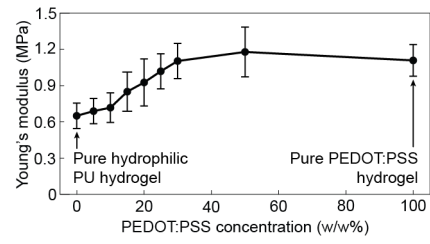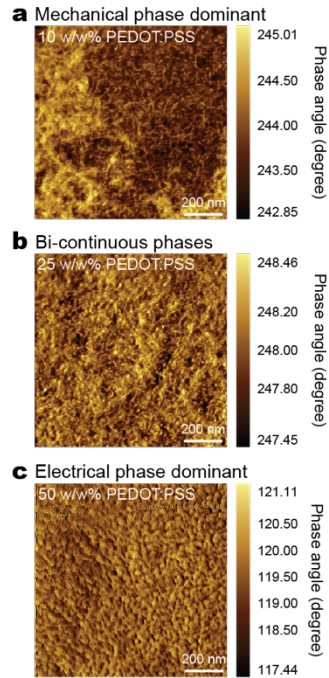
Supplementary Fig. 2 | Young's modulus of the BC-CPH with varying PEDOT:PSS concentrations.
Values represent the mean and the standard deviation ($n = 4$; independent samples).
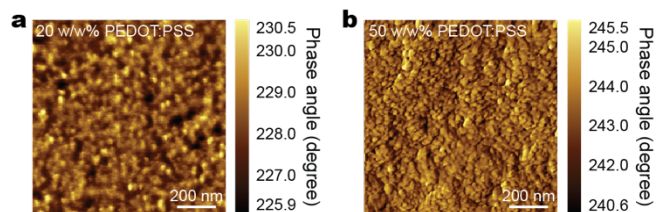
Supplementary Fig. 3 l AFM phase images of PVA-based conducting polymer hydrogels. a,b, AFM phase images of the PVA-based conducting polymer hydrogels with 20 w/w% (a) and 50 w/w% (b) PEDOT:PSS concentration. Each experiment was repeated independently 3 times.
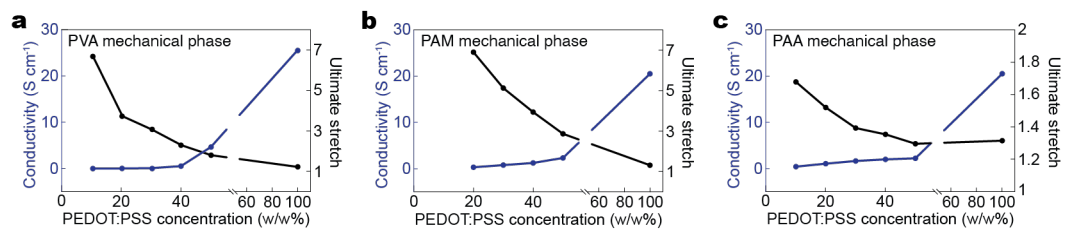
Supplementary Fig. 4 | Electrical and mechanical properties of conventional conducting polymer hydrogels. a-c, Plots for electrical conductivity (left axis) and ultimate stretch (right axis) vs. PEDOT:PSS concentration in conducting polymer hydrogels based on poly(vinyl alcohol) (PVA, a) polyacrylamide (PAM, b), and poly(acrylic acid) (PAA, c) mechanical phase.

a Mechanical phase dominant
10 w/w% PEDOT:PSS

Phase angle (degree)
245.01
244.50
244.00
243.50
242.85

200 nm

b Bi-continuous phases
25 w/w% PEDOT:PSS

Phase angle (degree)
248.46
248.20
248.00
247.80
247.45

200 nm

c Electrical phase dominant
50 w/w% PEDOT:PSS

Phase angle (degree)
121.11
120.50
120.00
119.50
119.00
118.50
117.44

200 nm

Supplementary Fig. 5 l AFM phase images of the BC-CPH with varying PEDOT:PSS concentrations.
a-c, AFM phase images of the BC-CPH with 10 w/w% (a), 25 w/w% (b), and 50 w/w% (c) PEDOT:PSS concentration. Each experiment was repeated independently 3 times.
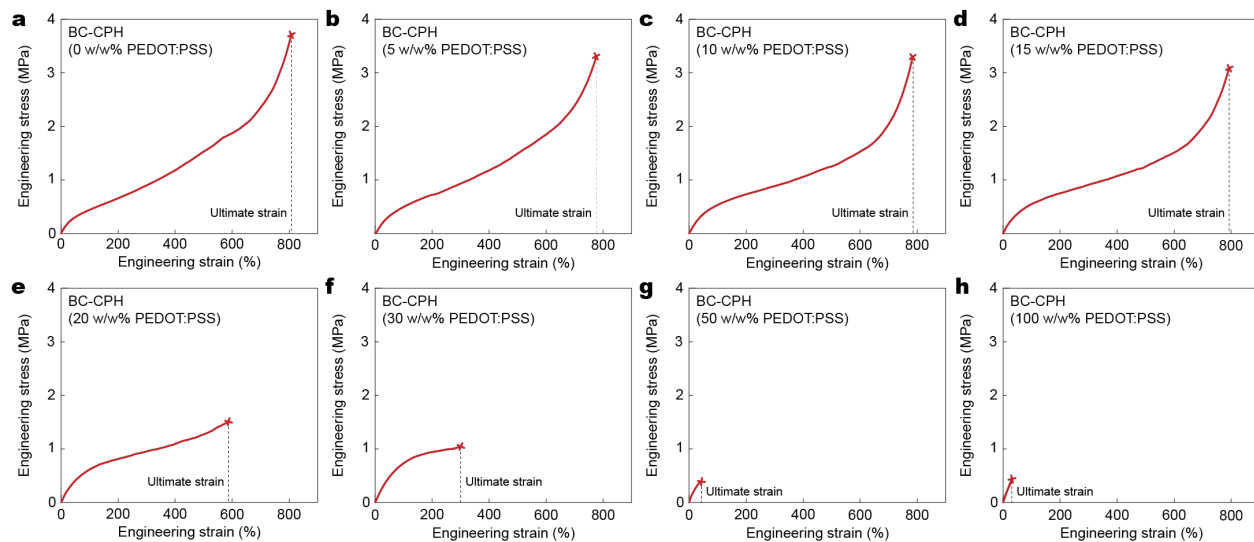
Supplementary Fig. 6 | Mechanical properties of the BC-CPH with varying PEDOT:PSS concentrations. a-h, Engineering stress vs. engineering strain curves for the BC-CPH with 0 w/w% (a), 5 w/w% (b), 10 w/w% (c), 15 w/w% (d), 20 w/w% (e), 30 w/w% (f), 50 w/w% (g), and 100 w/w% (h) PEDOT:PSS concentration.
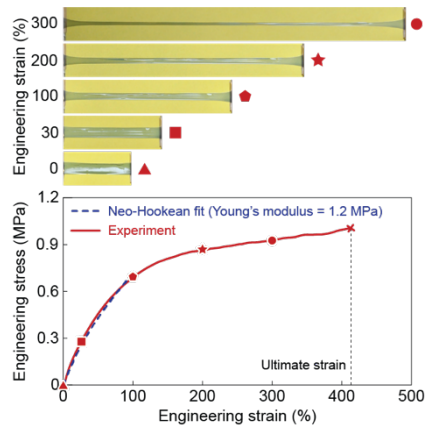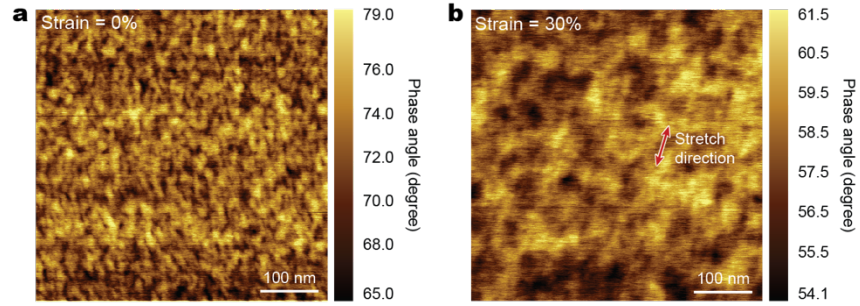
Supplementary Fig. 7 l High stretchability of the BC-CPH. Images (top) and plot for engineering stress vs. engineering strain (bottom) for the BC-CPH. Symbols (▲,■,⬟,★,●) on the plot correspond to the images at each strain. The BC-CPH with 25 w/w% PEDOT:PSS is used.
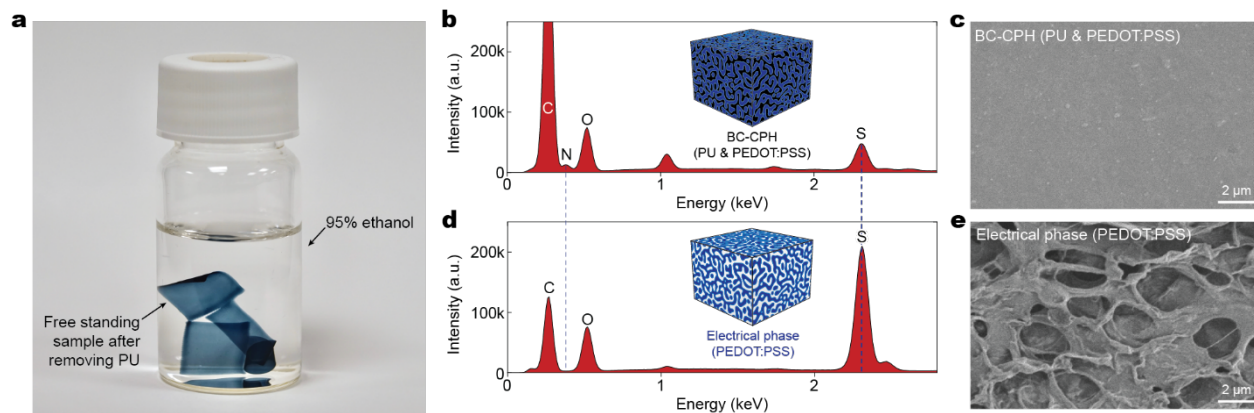
Supplementary Fig. 8 | Removal of mechanical phase from the BC-CPH. a, Image of the BC-CPH after removal of hydrophilic polyurethane (PU) mechanical phase. **b,c**, Energy-dispersive X-ray spectroscopy (EDS) spectra (b) and the representative SEM image (c) of the BC-CPH. **d,e**, EDS spectra of the BC-CPH (d) and the representative SEM image (e) of the BC-CPH after removal of mechanical phase. Each experiment was repeated independently 4 times.
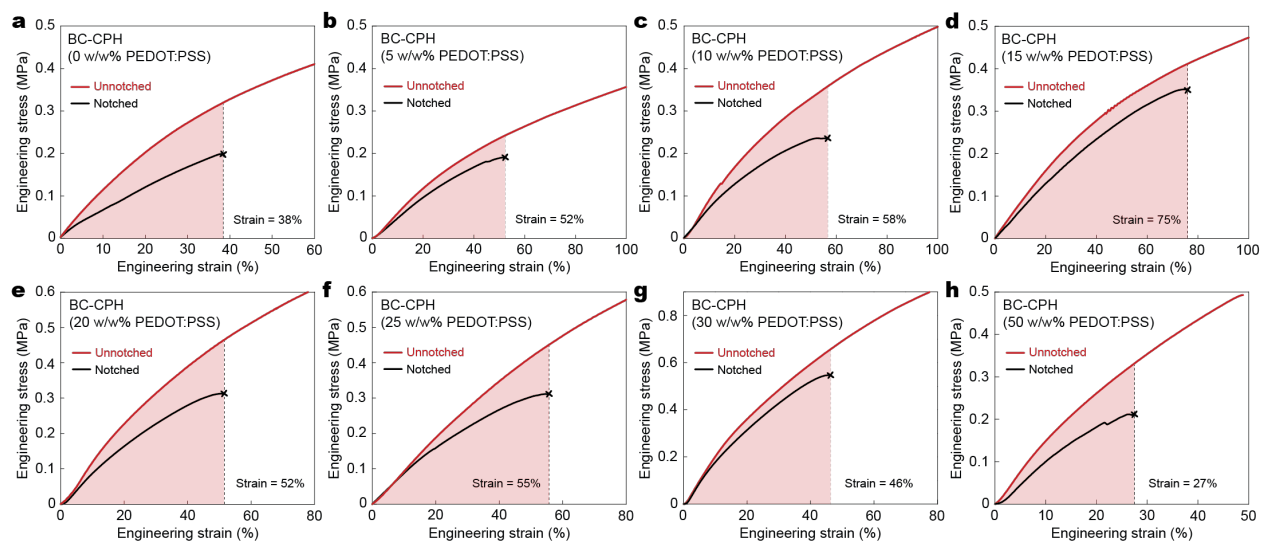
Supplementary Fig. 9 | Fracture toughness of the BC-CPH with varying PEDOT:PSS concentrations.
a-h, Engineering stress vs. engineering strain curves for the unnotched and notched BC-CPH with 0 w/w% (a), 5 w/w% (b), 10 w/w% (c), 15 w/w% (d), 20 w/w% (e), 25 w/w% (f), 30 w/w% (g), and 50 w/w% (h) PEDOT:PSS concentration.
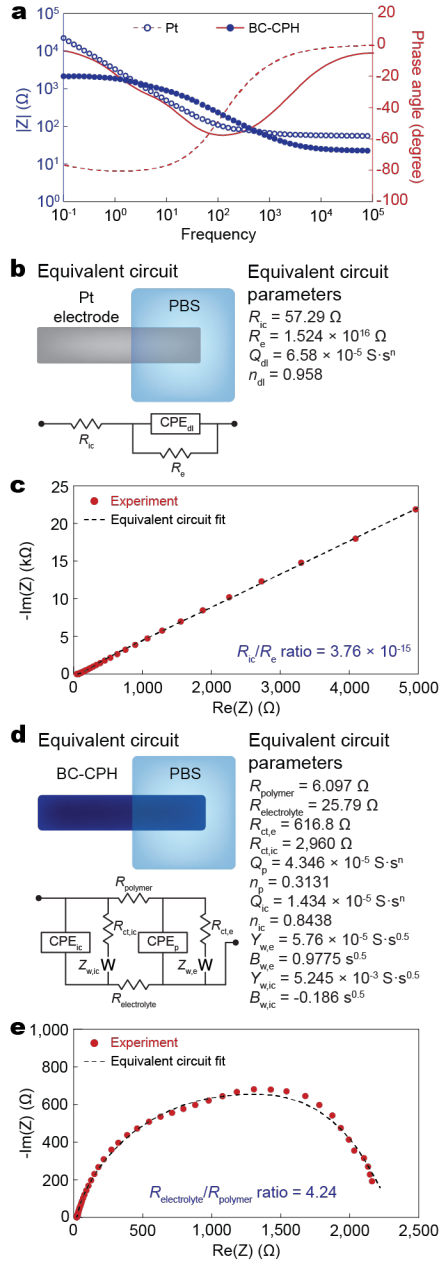
Supplementary Fig. 10 | Electrical properties of Pt electrode and the BC-CPH. a, Impedance (circle symbols, left axis) and phase angle (lines, right axis) vs. frequency plots for a Pt electrode and the BC-CPH. **b,c**, Equivalent circuit and parameters (b) and Nyquist plot (c) for a Pt electrode. R_{ic} represents the electronic resistance of the interconnect, R_e represents the electronic resistance of the Pt electrode, and CPE_{dl} represents the double-layer capacitive phase element (CPE) of the Pt electrode. **d,e**, Equivalent circuit and parameters (d) and Nyquist plot (e) for the BC-CPH. $R_{polymer}$ represents the electronic resistance of the BC-CPH, $R_{electrolyte}$ represents the ionic resistance of the electrolyte (PBS), $R_{ct,ic}$ represents the interconnect reaction resistance, $R_{ct,e}$ represents the electrode reaction resistance, CPE_{ic} represents the double-layer CPE of the interconnect, CPE_p represents the double-layer CPE of the BC-CPH, $Z_{w,ic}$ represents the interconnect Warburg element, and $Z_{w,e}$ represents the electrode Warburg element. CPE is used to account inhomogeneous or imperfect capacitance and are represented by the parameters Q and n where Q represents the peudocapacitance value and n represents the deviation from ideal capacitive behavior. The true capacitance C can be calculated from these parameters by using the relationship $C =$

$Q\omega_{max}{}^{n-1}$ where ω_{max} is the frequency at which the imaginary component reaches a maximum[25]. Warburg element is used to account diffusion circuit element and represented by the parameters Y and B where Y represents the admittance value and B represents the time constant of the diffusion circuit element. The impedance Z can be calculated from these parameters by using the relationship $Z(\omega) = \left(Y\sqrt{j\omega}\right)^{-1}\tanh\left(B\sqrt{j\omega}\right)$ where ω is the frequency[26].
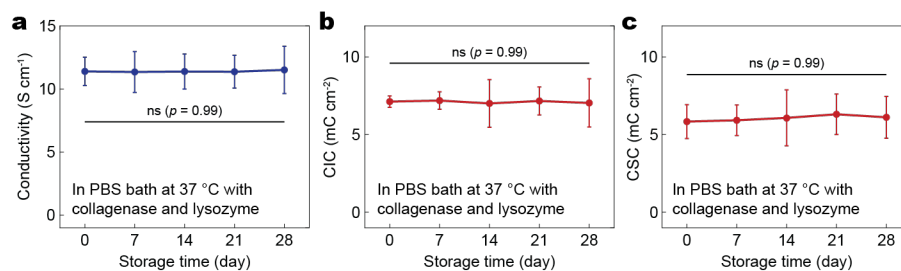
Supplementary Fig. 11 l Biodegradation of the BC-CPH. a-c, Electrical conductivity (a), charge injection capacity (CIC) (b), and charge storage capacity (CSC) (c) of the BC-CPH stored in PBS with collagenase and lysozyme at 37 °C. Values represent the mean and the standard deviation (n = 4; independent samples). One-way ANOVA followed by Bonferroni's multiple comparison test was used.

a Strain = 0%

79.0
76.0
74.0
72.0
70.0
68.0
65.0

Phase angle (degree)

100 nm

b Strain = 30%

61.5
60.5
59.5
58.5
57.5
56.5
55.5
54.1

Phase angle (degree)

Stretch direction

100 nm

Supplementary Fig. 12 l Electrical property of the BC-CPH under deformation. a,b, AFM phase images of the BC-CPH at engineering strain of 0% (a) and 30% (b). Arrow indicates the strain direction. The BC-CPH with 25 w/w% PEDOT:PSS is used. Each experiment was repeated independently 3 times.
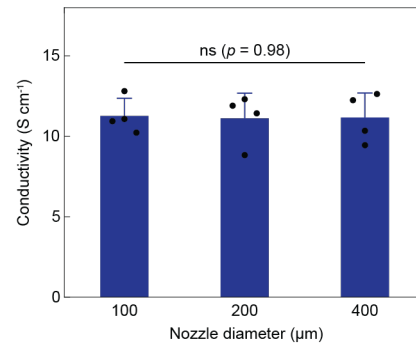
Supplementary Fig. 13 | Effect of printing nozzle size on the BC-CPH property. Values represent the mean and the standard deviation ($n = 4$; independent samples). Statistical significance and p values are determined by one-way ANOVA followed by Bonferroni's multiple comparison test; ns, not significant.
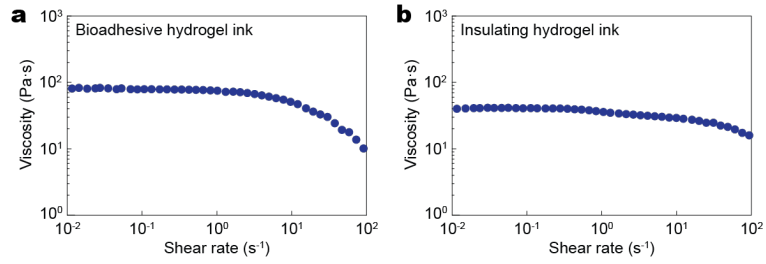
Supplementary Fig. 14 l Rheological property of the bioadhesive and insulating hydrogel inks. a,b, Viscosity vs. shear rate plots for the bioadhesive (a) and insulating (b) hydrogel inks.
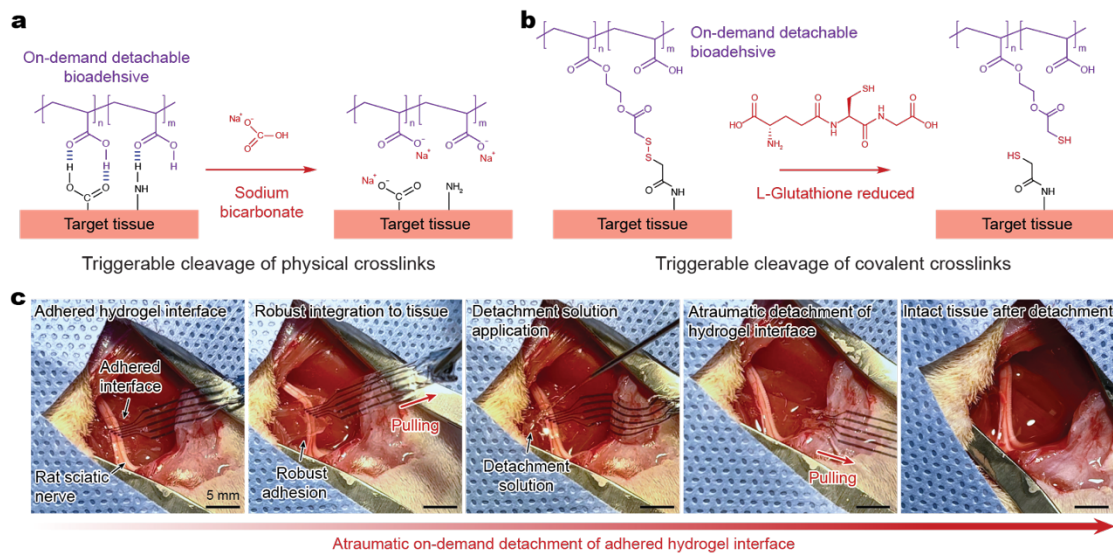
Supplementary Fig. 15 | On-demand detachment of the all-hydrogel bioelectronic interfaces. a,b, Schematic illustrations for the chemistry of on-demand detachment for physical crosslinks (a) and covalent crosslinks (b) between the bioadhesive hydrogel and the tissue surface. **c**, Snapshots of on-demand detachment of the all-hydrogel bioelectronic interface from a rat sciatic nerve.
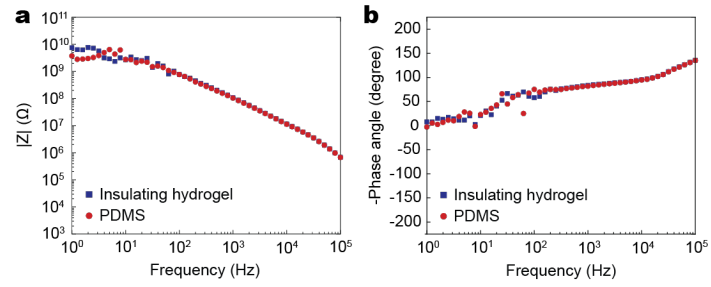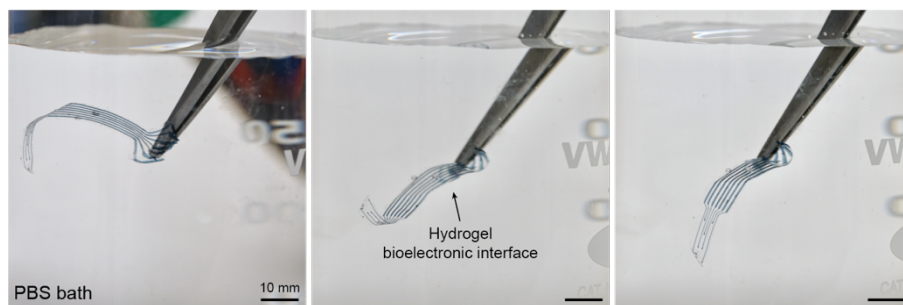
Supplementary Fig. 16 l Electrochemical property of the insulating hydrogel. a,b, Impedance (a) and phase angle (b) vs. frequency plots for a PDMS and the insulating hydrogel in PBS. The samples with 30 μm in thickness were used for both materials.
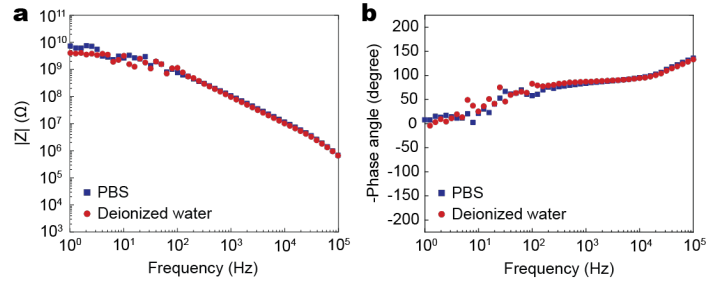
Supplementary Fig. 17 | Electrochemical property of the insulating hydrogel in PBS and deionized water. a,b, Impedance (a) and phase angle (b) vs. frequency plots for the insulating hydrogel measured in PBS (blue) and deionized water (red). The samples with 30 μm in thickness were used.
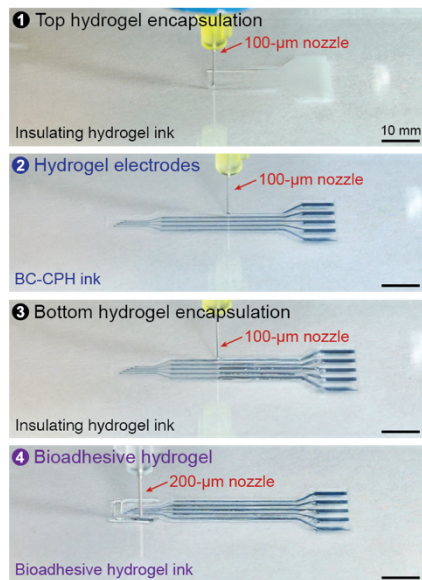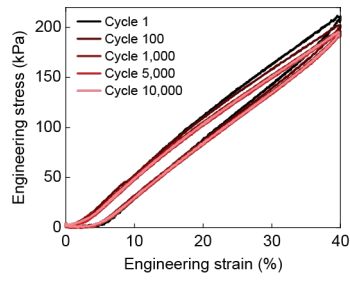
Supplementary Fig. 18 | Representative printing process of the all-hydrogel bioelectronic interface.
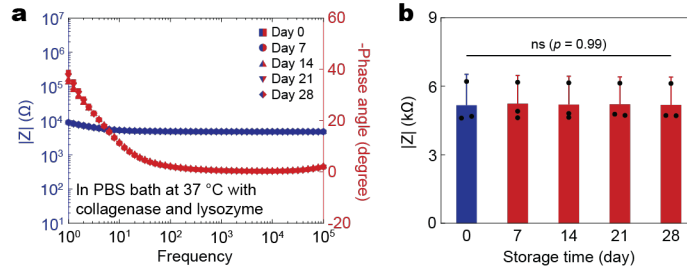
Supplementary Fig. 19 | All-hydrogel bioelectronic interface in PBS bath.
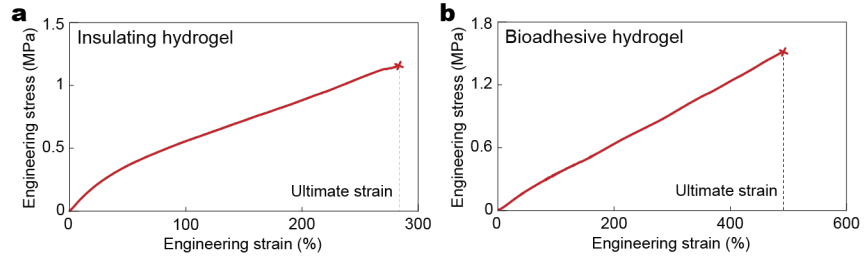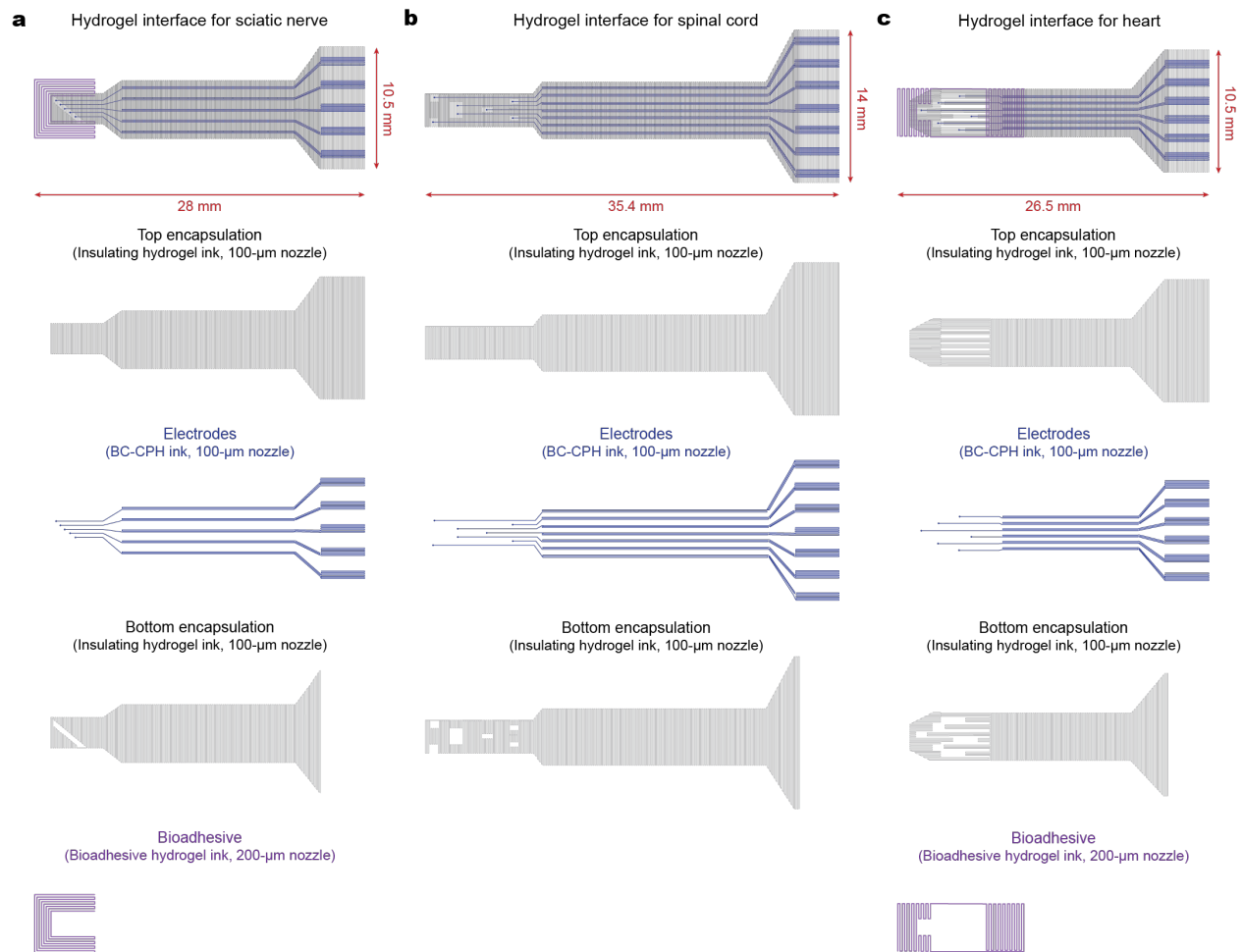
Supplementary Fig. 20 | Mechanical property of the insulating and bioadhesive hydrogels. a,b, Engineering stress vs. engineering strain plots for the insulating (a) and bioadhesive (b) hydrogels.

Supplementary Fig. 21 l Cyclic tensile tests of the all-hydrogel bioelectronic interface. Engineering stress vs. engineering strain plots for the hydrogel bioelectronic interface at different cycle numbers.
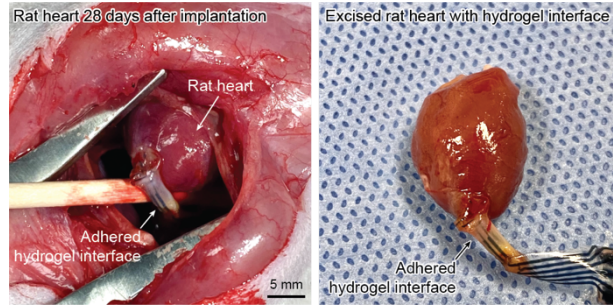
Supplementary Fig. 22 | Biodegradation of the all-hydrogel bioelectronic interface. a, Impedance (blue symbols, left axis) and phase angle (red symbols, right axis) vs. frequency plots for one electrode channel in the all-hydrogel bioelectronic interface stored in PBS with collagenase and lysozyme at 37 °C. **b**, Impedance of one electrode channel in the all-hydrogel bioelectronic interface at 1 kHz measured on different time points during the storage period. Values in **b** represent the mean and the standard deviation ($n = 3$; independent samples). Statistical significance and p values are determined by one-way ANOVA followed by Bonferroni's multiple comparison test; ns, not significant.
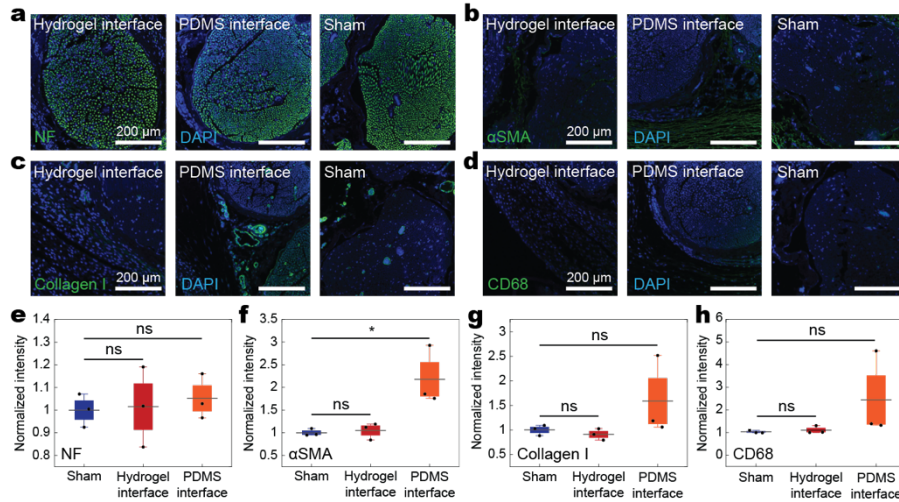
a Hydrogel interface for sciatic nerve

10.5 mm

28 mm

Top encapsulation
(Insulating hydrogel ink, 100-μm nozzle)

Electrodes
(BC-CPH ink, 100-μm nozzle)

Bottom encapsulation
(Insulating hydrogel ink, 100-μm nozzle)

Bioadhesive
(Bioadhesive hydrogel ink, 200-μm nozzle)

b Hydrogel interface for spinal cord

14 mm

35.4 mm

Top encapsulation
(Insulating hydrogel ink, 100-μm nozzle)

Electrodes
(BC-CPH ink, 100-μm nozzle)

Bottom encapsulation
(Insulating hydrogel ink, 100-μm nozzle)

c Hydrogel interface for heart

10.5 mm

26.5 mm

Top encapsulation
(Insulating hydrogel ink, 100-μm nozzle)

Electrodes
(BC-CPH ink, 100-μm nozzle)

Bottom encapsulation
(Insulating hydrogel ink, 100-μm nozzle)

Bioadhesive
(Bioadhesive hydrogel ink, 200-μm nozzle)

Supplementary Fig. 23 | Designs for the all-hydrogel bioelectronic interfaces for various target tissues. a-c, Overall designs and printing paths for the all-hydrogel bioelectronic interfaces for sciatic nerve (a), spinal cord (b), and heart (c).
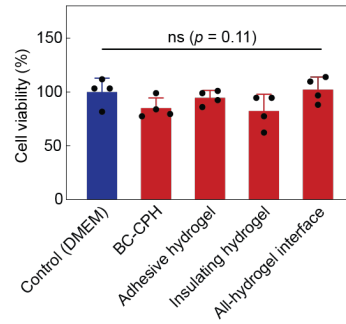
Supplementary Fig. 24 ǀ *In vitro* cytotoxicity. Cell viability of rat embryonic cardiomyocytes for control (DMEM), the BC-CPH, the adhesive hydrogel, the insulating hydrogel, and the all-hydrogel bioelectronic interface after 24-hour culture. DMEM, Dulbecco's modified eagle medium. Values represent the mean and the standard deviation ($n = 4$; independent samples). Statistical significance and p values are determined by one-way ANOVA followed by Bonferroni's multiple comparison test; ns, not significant.
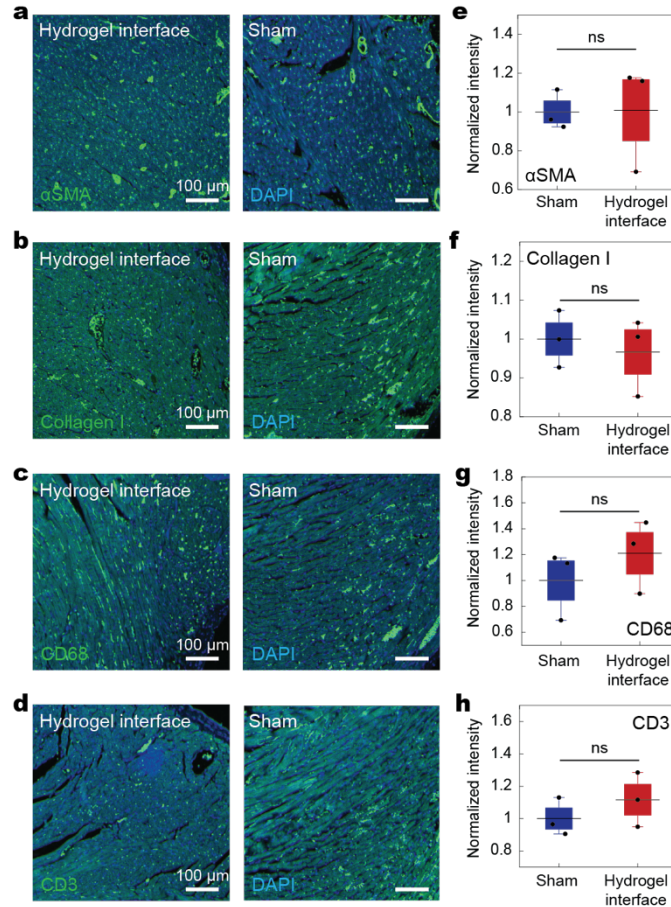
Supplementary Fig. 25 l *In vivo* **stability of bioadhesive integration of the all-hydrogel bioelectronic interface.** Images of the all-hydrogel bioelectronic interface adhered on a rat heart in *in vivo* (left) and in the excised heart (right) on day 28 post-implantation.
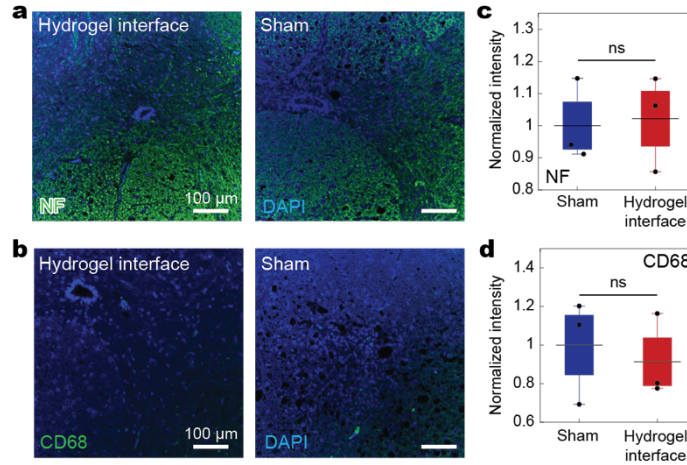
Supplementary Fig. 26 | Immunofluorescence analysis of rat sciatic nerve on day 7 post-implantation. a-d, Representative immunofluorescence images of rat sciatic nerve on day 7 post-implantation of the all-hydrogel bioelectronic interface, PDMS interface, and sham group (no device implantation). Each experiment was repeated independently for 3 times. Cell nuclei are stained with DAPI (blue). Green fluorescence corresponds to the expression of neurofilament (NF, a), fibroblasts (αSMA, b), collagen (collagen I, c), and macrophages (CD68, d), respectively. **e-h**, Normalized fluorescence intensity plots for the expression of NF (e), αSMA (f), Collagen I (g), and CD68 (h) in different groups. In box plots (e-h), center lines represent mean, box limits delineate standard error (SE), and whiskers reflect 5th and 95th percentile (n = 3; independent biological replicates). Statistical significance and p values are determined by two-sided unpaired t-test; ns, not significant; * $p < 0.05$. P values are 0.45, 0.20, 0.18, 0.029, 0.24, 0.083, 0.28, 0.051, respectively from left to right in (e) to (h).
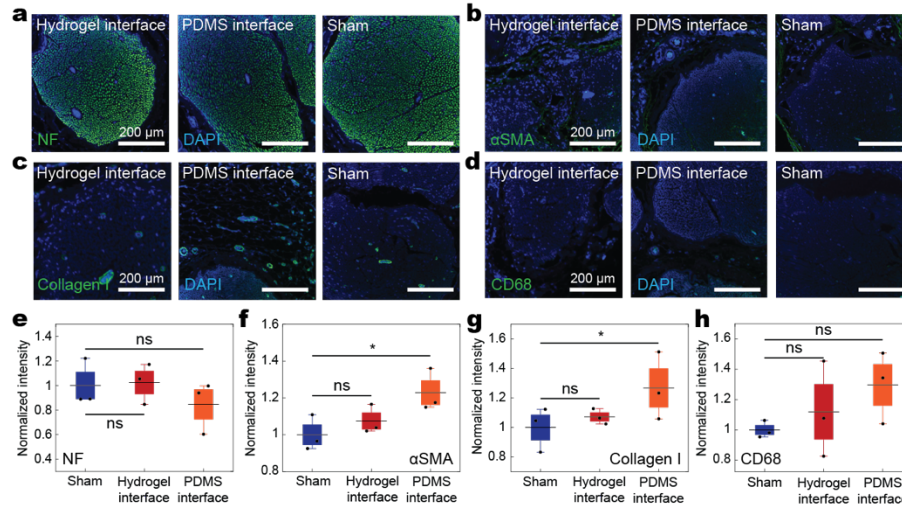
Supplementary Fig. 27 | Immunofluorescence analysis of rat sciatic nerve on day 56 post-implantation. a-d, Representative immunofluorescence images of rat sciatic nerve on day 56 post-implantation of the all-hydrogel bioelectronic interface, PDMS interface, and sham group (no device implantation). Each experiment was repeated independently for 3 times. Cell nuclei are stained with DAPI (blue). Green fluorescence corresponds to the expression of neurofilament (NF, a), fibroblasts (αSMA, b), collagen (collagen I, c), and macrophages (CD68, d), respectively. **e-h**, Normalized fluorescence intensity plots for the expression of NF (e), αSMA (f), Collagen I (g), and CD68 (h) in different groups. In box plots (e-h), center lines represent mean, box limits delineate standard error (SE), and whiskers reflect 5th and 95th percentile (*n* = 3; independent biological replicates). Statistical significance and *p* values are determined by two-sided unpaired *t*-test; ns, not significant; * *p* < 0.05. P values are 0.44, 0.26, 0.35, 0.018, 0.19, 0.14, 0.26, 0.13, respectively from left to right in (e) to (h).

Supplementary Fig. 28 | Immunofluorescence analysis of rat heart. a-d, Representative immunofluorescence images of rat heart on day 28 post-implantation of the all-hydrogel bioelectronic interface and sham group (no device implantation). Each experiment was repeated independently for 3 times. Cell nuclei are stained with DAPI (blue). Green fluorescence corresponds to the expression of fibroblasts (αSMA, a), collagen (collagen I, b), macrophages (CD68, c), and T cells (CD3, d), respectively. **e-h**, Normalized fluorescence intensity plots for the expression of αSMA (e), Collagen I (f), CD68 (g), and CD3 (h) in different groups. In box plots (e,f,g,h), center lines represent mean, box limits delineate standard error (SE), and whiskers reflect 5th and 95th percentile ($n = 3$; independent biological replicates). Statistical significance and p values are determined by two-sided unpaired t-test; ns, not significant.

Supplementary Fig. 29 | Immunofluorescence analysis of rat spinal cord. a,b, Representative immunofluorescence images of rat spinal cord on day 28 post-implantation of the all-hydrogel bioelectronic interface and sham group (no device implantation). Each experiment was repeated independently for 3 times. Cell nuclei are stained with DAPI (blue). Green fluorescence corresponds to the expression of neurofilament (NF, a) and macrophages (CD68, b), respectively. **c,d**, Normalized fluorescence intensity plots for the expression of NF (c) and CD68 (d) in different groups. In box plots (c,d), center lines represent mean, box limits delineate standard error (SE), and whiskers reflect 5th and 95th percentile ($n = 3$; independent biological replicates). Statistical significance and p values are determined by two-sided unpaired t-test; ns, not significant.
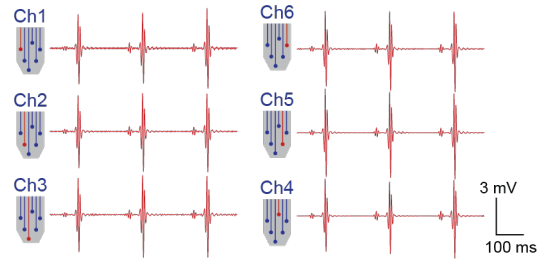
Supplementary Fig. 30 **| Epicardial recordings by different channels in the all-hydrogel bioelectronic interface on day 7 post-implantation.**
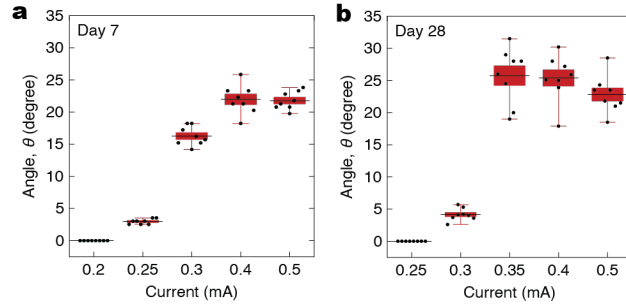
Supplementary Fig. 31 | Rat sciatic nerve stimulation on day 7 and day 28 post-implantation. a,b, Rat hindlimb movement angles upon sciatic nerve stimulations by the all-hydrogel bioelectronic interface at varying stimulation currents on day 7 (a) and day 28 (b) post-implantation. In box plots, center lines represent mean, box limits delineate standard error (SE), and whiskers reflect 5th and 95th percentile (*n* = 8; independent experiments).
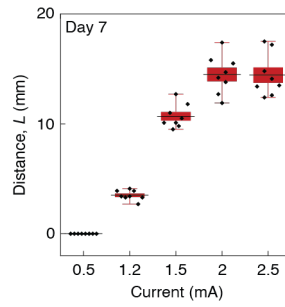
Supplementary Fig. 32 | Rat spinal cord stimulation on day 7 post-implantation. Rat forelimb movement distance upon spinal cord stimulations by the all-hydrogel bioelectronic interface at varying stimulation currents on day 7 post-implantation. In box plots, center lines represent mean, box limits delineate standard error (SE), and whiskers reflect 5th and 95th percentile ($n = 8$; independent experiments).
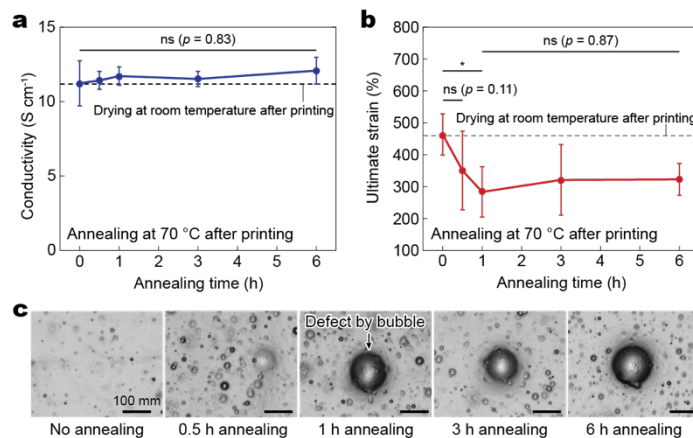
Supplementary Fig. 33 | Effect of annealing on the BC-CPH property. a,b, Electrical conductivity (a) and ultimate stretch (b) of the BC-CPH vs. annealing time at 70 °C. **c,** Microscopic images of the BC-CPH prepared with different annealing time at 70 °C. Each experiment was repeated independently for 4 times. Values in **a,b** represent the mean and the standard deviation ($n = 4$; independent samples). One-way ANOVA followed by Bonferroni's multiple comparison test was used. ns, not significant; * $p < 0.05$. P value in (b) is 0.03.

Supplementary Table 1 | Comparison between the BC-CPH and other conductive hydrogels

Conductive hydrogel	Conductivity (S m⁻¹)	Stretchability (%)	Toughness (J m⁻²)	Water contents (%)	Young's modulus (kPa)	Printability	Reference
Ionic hydrogels (high concentration salts)	1-10	300-500	10-100	> 90	100-1,000	Yes	Ref. 8
Au nanowire hydrogel	1-10	< 100	N/R	> 90	3.5	No	Ref. 14
CNT/graphene hydrogel	1-10	< 100	N/R	> 90	10-100	No	Ref. 15
PANi hydrogel (IPN with PVA)	5-9	140	N/R	80-90	120	No	Ref. 16
PEDOT:PSS hydrogel (IPN with PAA)	23	300	N/R	50-80	8-374	No	Ref. 17
PEDOT:PSS hydrogel (IPN with PAAm)	0.2	100	N/R	85-90	N/R	No	Ref. 18
PEDOT:PSS hydrogel (IPN with PVA)	1.8	400	N/R	80-90	800	Yes	Ref. 19
PEDOT:PSS hydrogel (composite with HPU)	6.35 (in DI water)	600	N/R	60	1,200	Yes	Ref. 20
PEDOT:PSS hydrogel (composite with PU/LCGO)	1,250	891	N/R	57	5,640	No	Ref. 21
PEDOT:PSS hydrogel (glycerol-based)	200	500 (Plastic deformation)	N/R	< 10	400	No	Ref. 22
PEDOT:PSS hydrogel (ionic liquid-based)	4,740 (in DI water)	30	N/R	82	32	No	Ref. 23
Pure PEDOT:PSS hydrogel (100 w/w% PEDOT:PSS)	2,000 (in PBS)	35	280	80	2,000	Yes	Ref. 24
BC-CPH (25 w/w% PEDOT:PSS)	**1,100 (in PBS)**	**400**	**3,300**	**76**	**900**	**Yes**	**This work**

N/R: Not reported

Supplementary References

1   Yuk, H. *et al.* Dry double-sided tape for adhesion of wet tissues and devices. *Nature* **575**, 169-174 (2019).

2   Deng, J. *et al.* Electrical bioadhesive interface for bioelectronics. *Nature Materials* **20**, 229-236 (2021).

3   Yuk, H., Zhang, T., Parada, G. A., Liu, X. & Zhao, X. Skin-inspired hydrogel–elastomer hybrids with robust interfaces and functional microstructures. *Nature Communications* **7**, 12028 (2016).

4   Yu, Y. *et al.* Multifunctional "hydrogel skins" on diverse polymers with arbitrary shapes. *Advanced Materials* **31**, 1807101 (2019).

5   Wu, S. J., Yuk, H., Wu, J., Nabzdyk, C. S. & Zhao, X. A multifunctional origami patch for minimally invasive tissue sealing. *Advanced Materials* **33**, 2007667 (2021).

6   Mao, X., Yuk, H. & Zhao, X. Hydration and swelling of dry polymers for wet adhesion. *Journal of the Mechanics and Physics of Solids* **137**, 103863 (2020).

7   Chen, X., Yuk, H., Wu, J., Nabzdyk, C. S. & Zhao, X. Instant tough bioadhesive with triggerable benign detachment. *Proceedings of the National Academy of Sciences* **117**, 15497-15503 (2020).

8   Yang, C. & Suo, Z. Hydrogel ionotronics. *Nature Reviews Materials* **3**, 125-142 (2018).

9   Yuk, H., Lu, B. & Zhao, X. Hydrogel bioelectronics. *Chemical Society Reviews* **48**, 1642-1667 (2019).

10   Pissis, P. & Kyritsis, A. Electrical conductivity studies in hydrogels. *Solid State Ionics* **97**, 105-113 (1997).

11   Konsta, A., Daoukaki, D., Pissis, P. & Vartzeli, K. Hydration and conductivity studies of polymer–water interactions in polyacrylamide hydrogels. *Solid State Ionics* **125**, 235-241 (1999).

12   Austin, D. & Kumar, R. Ionic conductivity in hydrogels for contact lens applications. *Ionics* **11**, 262-268 (2005).

13   Lin, J., Chen, H. & Xu, W. Geometrical percolation threshold of congruent cuboidlike particles in overlapping particle systems. *Physical Review E* **98**, 012134 (2018).

14   Dvir, T. *et al.* Nanowired three-dimensional cardiac patches. *Nature Nanotechnology* **6**, 720-725 (2011).

15   Tringides, C. M. *et al.* Viscoelastic surface electrode arrays to interface with viscoelastic tissues. *Nature Nanotechnology* **16**, 1019–1029 (2021).

16   Zhao, Y. *et al.* Hierarchically structured stretchable conductive hydrogels for high-performance wearable strain sensors and supercapacitors. *Matter* **3**, 1196-1210 (2020).

17   Feig, V. R., Tran, H., Lee, M. & Bao, Z. Mechanically tunable conductive interpenetrating network hydrogels that mimic the elastic moduli of biological tissue. *Nature Communications* **9**, 2740 (2018).

18   Dai, T. *et al.* Mechanically strong conducting hydrogels with special double-network structure. *Synthetic Metals* **160**, 791-796 (2010).

19   Wei, H. *et al.* Orthogonal photochemistry-assisted printing of 3D tough and stretchable conductive hydrogels. *Nature Communications* **12**, 2082 (2021).

20   Naficy, S., Oveissi, F., Patrick, B., Schindeler, A. & Dehghani, F. Printed, flexible pH sensor hydrogels for wet environments. *Advanced Materials Technologies* **3**, 1800137 (2018).

21   Javadi, M. *et al.* Conductive tough hydrogel for bioapplications. *Macromolecular Bioscience* **18**, 1700270 (2018).

22   Liu, Y. *et al.* Morphing electronics enable neuromodulation in growing tissue. *Nature Biotechnology* **38**, 1031-1036 (2020).

23   Liu, Y. *et al.* Soft and elastic hydrogel-based microelectronics for localized low-voltage neuromodulation. *Nature Biomedical Engineering* **3**, 58-68 (2019).

24   Lu, B. *et al.* Pure Pedot: Pss hydrogels. *Nature Communications* **10**, 1043 (2019).

25   Hsu, C. H. & Mansfeld, F. Concerning the conversion of the constant phase element parameter Y 0 into a capacitance. *Corrosion* **57**, 747-748 (2001).

26   Jacobsen, T. & West, K. Diffusion impedance in planar, cylindrical and spherical symmetry. *Electrochimica Acta* **40**, 255-262 (1995).